Multiscale image-based modelling of composite materials

Dongze He, Yang Chen, Christian Breite, Mikhail Y Matveev, Léonard Turpin, Elena Syerko, Guillaume Couégnat, Jeroen Soete, Mahoor Mehdikhani, Stepan V Lomov, et al.

Review

ASM INTERNATIONAL

I·M3 Institute of Materials, Minerals & Mining

Multiscale image-based modelling of composite materials

International Materials Reviews
1–33

DOI: 10.1177/09506608251363653
journals.sagepub.com/home/inr

Dongze He[1], Yang Chen[2], Christian Breite[3], Mikhail Y Matveev[4], Léonard Turpin[5,6], Elena Syerko[7], Guillaume Couégnat[8], Jeroen Soete[3], Mahoor Mehdikhani[3], Stepan V Lomov[3], Yentl Swolfs[3] and Philip J Withers[1,9]

Abstract

By control of their constituents, interfaces and architectures, composite materials can display a much broader suite of beneficial material properties than is possible for single-phase materials. Furthermore, advanced manufacturing techniques are increasing the freedom to operate of composite designers. While much can be achieved with idealised models of composites, models are needed that more accurately reflect the non-ideal placement of reinforcement, matrix-free regions and manufacturing defects that occur in practice. At the same time, imaging techniques, and X-ray computed tomography in particular, have radically increased the level of information that can be obtained in three dimensions and over time about real composite microstructures, both about the as-manufactured condition and their behaviour in-service. This review considers all aspects of image-based modelling of composite materials across the length scales. It also discusses establishing the appropriate constitutive equations for deterministic and stochastic (e.g., fibre fractures) elements of behaviour, as well as methods for validation. A range of actual and potential applications from the literature are showcased throughout. It explores approaches to bridging the scales and techniques, such as surrogate and homogenised models, to ensure models are computationally feasible. It covers a wide range of composites, spanning polymer, metal and ceramic matrices, continuous and short fibres, as well as particulate reinforcements. It also briefly extends to how such approaches can be applied to other 'composite' systems, such as concrete and hard metals. Overall, this is a one-stop review for those considering multiscale modelling of composites based on realistic, often multiscale, composite architectures.

Keywords

polymer matrix composites (CFRP and GFRP), finite element modelling, metal matrix composites (MMCs), ceramic matrix composites (CMCs), digital twin

Received: 15 May 2024; accepted: 15 July 2025

Introduction

Composite materials offer almost limitless scope for the design of material architectures that bring together the attributes of different phases to deliver properties that can be anisotropic, and that can be varied locally to optimise performance across a component or structure. In addition, the various interfaces within a composite can be controlled to deliver functionalities not even possessed by the constituents that make them up (e.g., tough ceramic composites from brittle constituents). Nowhere is this design freedom more evident than in nature,[1] where composites rule supreme, delivering a range of useful properties from quite ordinary constituents through complex hierarchical structures from the Bouligand structures giving rise to the iridescence of beetles,[2] to the interdigitated layers comprising co-oriented needles, plates, and a polycrystalline matrix conferring upon sea urchin teeth the self-sharpening wear resistance needed to grind rocks.[3]

[1]Henry Royce Institute, Department of Materials, The University of Manchester, Manchester, UK
[2]Department of Mechanical Engineering, University of Bath, Bath, UK
[3]Department of Materials Engineering, KU Leuven, Leuven, Belgium
[4]Composites Research Group, Faculty of Engineering, University of Nottingham, Nottingham, UK
[5]Diamond Light Source, Didcot, UK
[6]Univ. Bordeaux/CNRS/Bordeaux INP, I2M, UMR 5295, Talence, France
[7]Research Institute in Civil Engineering and Mechanics (GeM), Nantes Université, Ecole Centrale Nantes, CNRS, GeM, UMR 6183, Nantes, France
[8]Laboratoire des Composites Thermostructuraux, UMR5801 CNRS/Univ. Bordeaux/Safran/CEA, Pessac, France
[9]Department of Materials Science and Engineering, Monash University, Clayton, Australia

Corresponding author
Philip J Withers, Henry Royce Institute, Department of Materials, University of Manchester, Oxford Rd, Manchester M13 9PL, UK.
Email: p.j.withers@manchester.ac.uk

This freedom to operate has yet to be widely explored in manufacturing despite the need for composite materials across aerospace, marine and many other sectors and the advent of 'additive' manufacturing methods that offer greater design flexibility. This is in part because we do not have the models needed to explore this space in detail. This problem is compounded by our reliance on an extensive and time-consuming testing pyramid (see Figure 1) requiring expensive sets of tests across the various length scales. Consequently, if we are to expand the use of composite materials and explore the opportunities they present, we need to enhance modelling capability across all length scales. This requires a digital twin for both composite manufacturing and for predicting composite performance. Many of the larger length scales can be modelled by finite element modelling, although the question of manufacturing defects and uncertainty require further attention. Here, we focus primarily on the scales relevant to modelling at the coupon scale. According to the reinforcement type and composite architecture, these range from modelling the matrix, reinforcement and interface, to the tow (fibre bundle level), to the textile or laminae scale to the coupon scale.

The simplest approach to composite modelling is to try to capture the essence of the composite without considering the separate phases explicitly through a continuum model (as illustrated in Figure 2(b)). In this case, the influence of the reinforcement is described using continuum composite laws. These can include continuum damage accumulation parameters. To capture the influence of the interface, the phases must normally be included explicitly, and the computationally simplest way of doing this is via an idealised unit cell taken to repeat many times throughout the composite (see Figure 2(c)). In the case illustrated, the properties of the 'matrix' could be adapted to consider the effect of the fine scale pores visible in Figure 2(a). As to whether the simplest unit cell is sufficient may depend on whether volume-averaged properties, such as stiffness, are required or properties more dependent on local aspects, such as damage or fracture. It can also depend on whether composite variability and/or manufacturing defects need to be incorporated into the representative volume element (RVE). In many cases, the RVE, or sometimes the statistically equivalent RVE,[5] which is the smallest volume that must be modelled to accurately capture the behaviour of interest, must be considerably bigger than an idealised unit cell. Either synthetic or imaged-based RVEs of increasing complexity and size can be employed (see Figure 2(d)–(f)), but at the cost of significantly increased computational demands. Often, 3D image-based models are generated from 2D Scanning Electron Microscope (SEM) images such as that in Figure 2(a), although 3D models based on X-ray Computed Tomography (X-CT) are becoming more common. Indeed, it is sometimes referred to as X-ray tomography aided engineering.

In practice, a combination of these approaches is often employed in multiscale modelling (see sub-section: *Multiscale modelling*). For instance, an image-based model can be used to capture the defects and arrangement of fibres within a laminate, while a continuum model is used to carry these properties over into a laminate and then to the component scale.

This review covers all the processes needed to construct, apply and validate image-based modelling from the capturing of image data, building the models and the underlying constitutive equations to their application in manufacturing and the prediction of in-service properties. It is relevant to the modelling of a wide range of reinforcement morphologies. This includes the particulate reinforcements typical of discontinuous metal matrix composites, hard metals (cemented carbides) and cementitious materials (e.g., concrete). While in some cases, the level of particulate reinforcement is varied through the component, generally, such composites do not require consideration of any longer microstructural length scales, and so image-based models can be relatively small. Polymer-matrix short-fibre systems are attracting increasing interest due to their ease of manufacture and recycling, as well as their ability to use recycled fibres. These introduce the complexity of anisotropy. Much of the

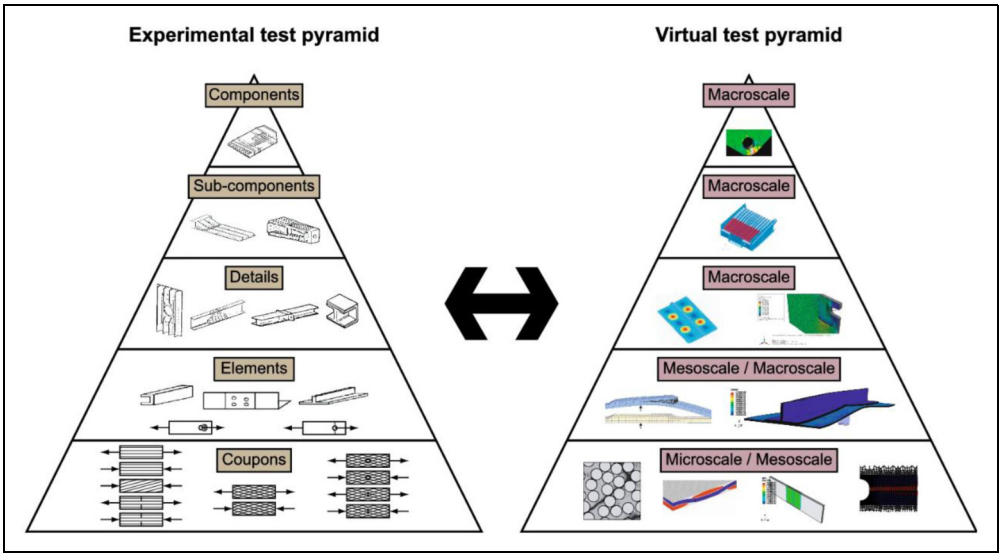

Figure 1. To lower the cost of composite manufacturing and certification, the multiscale experimental test pyramid needs to be complemented by its digital twin.[4]

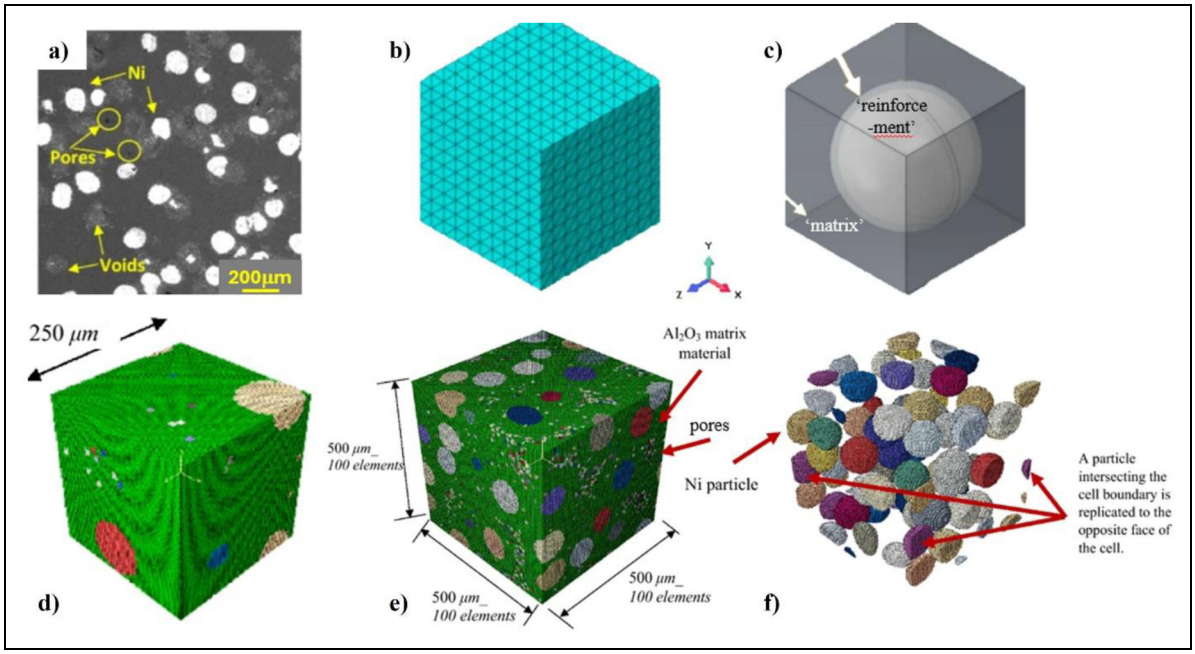

Figure 2. (a) A 2D SEM image of a sintered Ni particle/ Al_2O_3 matrix composite, (b) a continuum representation exploiting a composite model, (c) a simple idealised unit cell, (d) small (125,000 elements) and (e) larger (1 million elements) representative volume elements that capture many features of the composite, and f) periodic nature of RVEs created by DREAM.3D from the 2D image in (a) (images from[6]).

review is focused on long fibre composites, mainly polymer and ceramic matrix composite systems. The fibres can be arranged in the form of various textiles as well as in laminae, resulting in the need to produce complex multiscale models. Layered composites building on natural examples, such as nacre, are also being explored as a means of making tougher high-temperature ceramic composites, while structured (lattices) and unstructured (foam) porous materials can be thought of as air composites and are also benefiting from microstructural design through image-based modelling. Some of these composite systems are discussed in the Applications *p* section.

Capturing image data

The first step of image-based modelling is to collect realistic images that capture the key features at the appropriate scale(s). This could be of the whole component or only a small sample that is needed to generate an RVE to form an image-based sub-model.[7] X-ray imaging methods can now provide 3D images of unparalleled detail,[8] but in some cases, it is sufficient, simpler, and more cost-effective to capture 2D images and to use these as the basis for 3D modelling.

2D microscopy of composites

Much of what we have learnt about structure/property relationships in composite materials has been gained from optical or scanning electron imaging of composite sections.[9] Great care must be taken when sectioning to avoid introducing artefacts. Two-dimensional imaging methods are generally much cheaper than their 3D equivalents, and one can examine large areas at high resolution to help ensure their representativeness. Three-dimensional quantities such as fibre orientation[10] and length[11] distributions can be obtained from these sections, often by analysing images taken at multiple depths, or in perpendicular directions at selected locations by a process called stereology, which has been reviewed for composites by Lukas and Chaloupek.[12]

In some cases, 2D image-based models are sufficient, for example when modelling well-aligned long fibre materials or isotropic particulate materials such as concrete.[13] In other cases, sufficiently realistic 3D images can often be inferred directly from the 2D images. Indeed, some software, such as DREAM 3D[14] (now DREAM3D-NX), can create realistic 3D microstructures from quantities (e.g., particle size, shape distribution and the radial distribution function) obtained directly from 2D images, as shown in Figure 2. One of the first codes to do this was CEMHYD3D,[15] designed to create 3D cementitious RVE microstructures. Recently, a generative machine learning algorithm called sliceGAN[13] has been developed to create realistic 3D images from a single 2D slice in cases where the properties are isotropic (Figure 3(b)), or from two or more perpendicular planes when they are not (Figure 3(c)).

It is also possible to combine serial sectioning with scanning electron or optical imaging to create 3D image volumes using ion beams (100 μm sized volumes),[16] laser beams (mm volumes)[17,18] or mechanical sectioning methods[19] (10–100 s of mm volumes). While such methods can be used to create an image stack sufficient to create an image-based sub-model of, say, the fibres within a laminate, only mechanical sectioning is really of a length scale suited to creating meso- or macroscale models of woven or composite laminate architectures.[20]

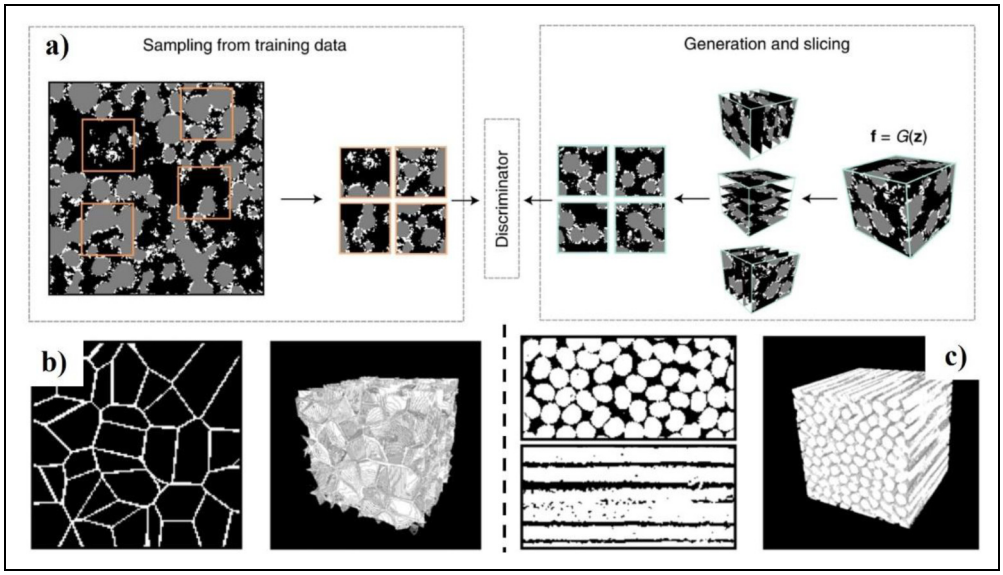

Figure 3. Inferring 3D images from a 2D image, (a) first, real images are sampled from the 2D training sample, a fake volume is then generated and sliced along *x*, *y* and *z*. This yields a compatible pair of datasets, which can both be fed to a 2D discriminator. Exemplar binarised training data (left hand image) and inferred 3D volume (right hand image) for (b) a cellular foam and (c) a fibre composite.[13]

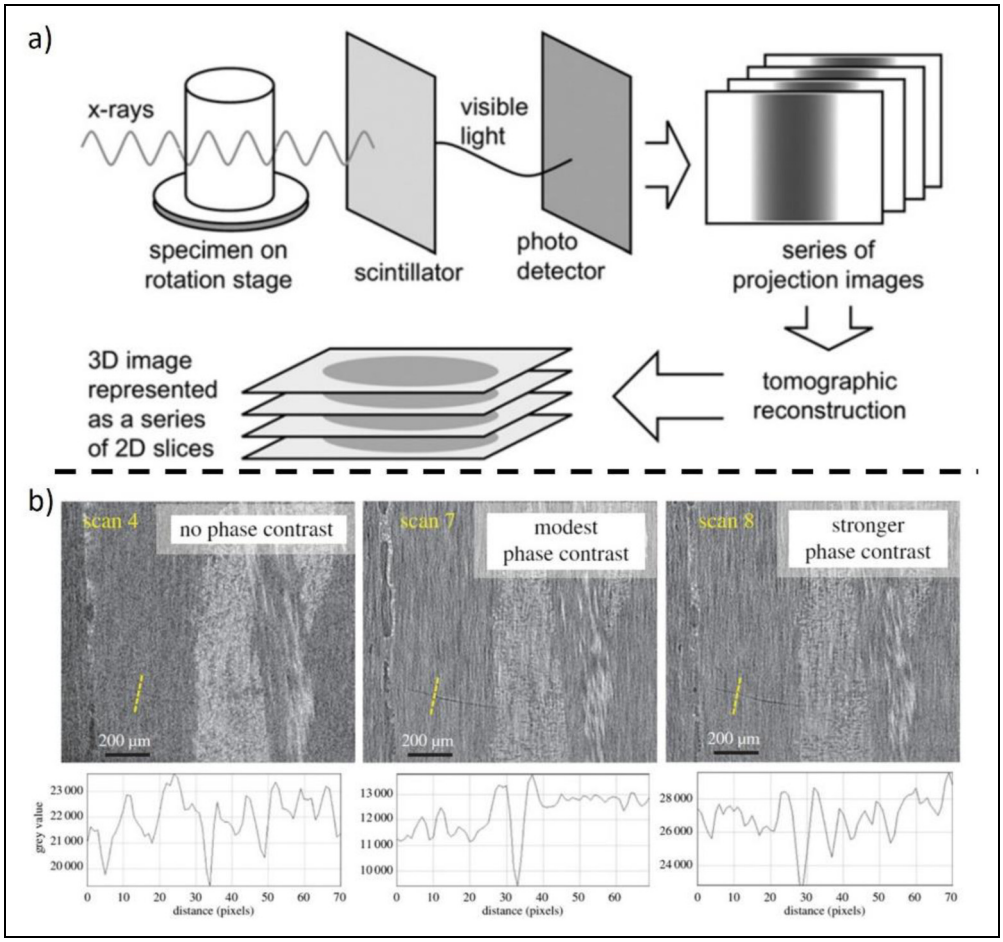

Figure 4. (a) schematic illustrating the X-CT image acquisition process[24] and (b) three virtual X-CT slices corresponding to the same plane in a 3D glass-fibre woven composite without phase contrast, with modest in-line phase contrast and with stronger phase contrast. The grey scale line profiles correspond to the dashed yellow line.[25]

X-ray computed tomography (X-CT)

With the increasing demand for real-time 3D characterisation and advancements in spatial resolution, X-CT has emerged as a powerful tool for multiscale imaging (micro-, meso- and macroscale) of composite structures, manufacturing defects and in-service damage.[21–23] Figure 4(a) shows how a series of X-ray radiographs, or projections, of a sample acquired as it is rotated can be processed using a reconstruction algorithm to obtain a 3D image of the specimen. We usually distinguish two kinds of tomography: laboratory (or lab) tomography, using an X-ray tube as source, and synchrotron tomography using a synchrotron light source. Lab sources generally provide a conical beam containing a range of X-ray energies depending on the accelerating voltage and target material, while synchrotron sources usually provide a parallel beam that is more brilliant, enabling significantly shorter acquisition times.

Two contrast modes are possible in conventional X-CT: a) absorption (or attenuation) contrast, which is the most common and is available with both laboratory and synchrotron sources; and b) phase-contrast, which requires a coherent beam and usually requires a synchrotron source.[8] They derive from the imaginary (β) and real (δ) parts of the refractive index, n, which is usually written as,

$$n = 1 - \delta + i\beta \tag{1}$$

Absorption contrast results from the reduction of intensity of X-rays as they pass through the sample constituents, absorption tomography is then an image of the local attenuation coefficient $\mu(x,\ y,\ z)$. The attenuation coefficient broadly varies (neglecting absorption edges) as[8,23]:

$$\mu(x,\ y,\ z) \sim \rho \frac{Z}{E^3} \tag{2}$$

where ρ is the material density, Z and E respectively are the material's atomic number and the X-ray beam energy. This means that samples containing mainly high atomic number elements require higher X-ray energies, while softer materials require lower energy X-rays to achieve good transmission and contrast. Consequently, the energy of the incoming beam is usually chosen to maximise the absorption contrast. In this respect, the large differences in attenuation coefficient between the constituents mean that absorption contrast is then well suited to glass fibre-reinforced polymer (GFRP) composite or metal matrix composite (MMC) imaging. The imaging of carbon fibre-reinforced polymers (CFRPs) or ceramic matrix composites (CMCs), where the absorption contrast between the fibres and the matrix is low, is more challenging (see for example Figure 4(b)).

X-ray phase contrast[8] imaging is particularly useful for weakly attenuating materials,[21] as material interfaces can be enhanced by detecting the phase shifts. Several experimental approaches exist for detecting phase shifts. The simplest is propagation-based phase-contrast imaging (also called in-line phase contrast imaging),[26,27] which arises when the beam is sufficiently coherent, usually using synchrotron radiation, and the sample-to-detector distance is large enough (see Figure 4(b)). Phase contrast imaging provides enhanced edge definition and improved feature detectability in carbon fibre-reinforced polymer (CFRP) composites, as shown in Figure 4(b). In practice, the measured image is a combination of phase and absorption contrast, their contribution can be tuned *a posteriori* using filters, such as a Paganin filter.[28]

The spatial resolution of X-CT images is generally around 2–3 pixels.[21] For a given pixel size, the field of view is limited by the size of the detector (typically a 4–12 mega-pixel array). However, by stitching projections or volumes together, the field of view can be increased (at the cost of a higher acquisition time).[29] In many cases, the main limitation is not the acquisition of the images, but the processing of the huge volume data. Given the multiscale nature of many composites, this limitation must be borne in mind alongside the computation limits when choosing what aspects of the composite require image-based methods, e.g., the arrangement of the individual fibres, the fibre tows, or the individual laminates.

As illustrated in section: Applications, a key advantage of X-CT over destructive sectioning is that it allows repeated 3D imaging to follow structural changes during manufacturing, or in response to in-service environments or loading histories. This can be done by continuous capture whereby the sample is continuously rotated relative to the X-ray source, or by in-situ or ex-situ time-lapse imaging to monitor longer timescale events. In general terms, synchrotron beamlines are better suited to short timescale, microscale, small sample studies, while lab sources are better suited to longer timescale and larger specimen/component studies. In both cases, this means that X-CT is not just an excellent means of setting up image-based modelling strategies but also for validating the predictive capability of the resulting models (see sub-section: *Validation with experimental results*).

Small-angle scattering tensor tomography

It is often not feasible to image individual fibres at sufficient resolution, or with sufficient contrast, by X-CT to segment them individually. In such cases, indirect methods come into play, for example exploiting two-dimensional small-angle X-ray scattering (SAXS) to reveal microstructural anisotropy.[30–34] One means of doing this is to use an array of circular gratings[32,35] (see Figure 5(a)), enabling anisotropic scattering information to be extracted at each image pixel by measuring the change in the circular fringes before and after inserting the sample into the beam path. After reconstructing the local 2D small-angle X-ray scattering signal, scattering tensors describing the local 3D scattering character of each voxel within the sample[33,34] can be computed from which the degree of fibre orientation in 3D can be inferred,[32,35] as shown in Figure 5.

Building image-based models

Except when modelling the whole component, a key question is how big a region is needed to represent the composite at the length scale of interest. Computational complexity and imaging limits typically prohibit image-based modelling across all three length scales (micro-, meso- and macroscale) simultaneously. As a result, hybrid approaches combining image-based models with continuum models are common. In this context, it is critical to choose a 2D area, or a 3D image volume, that is large enough to be representative of

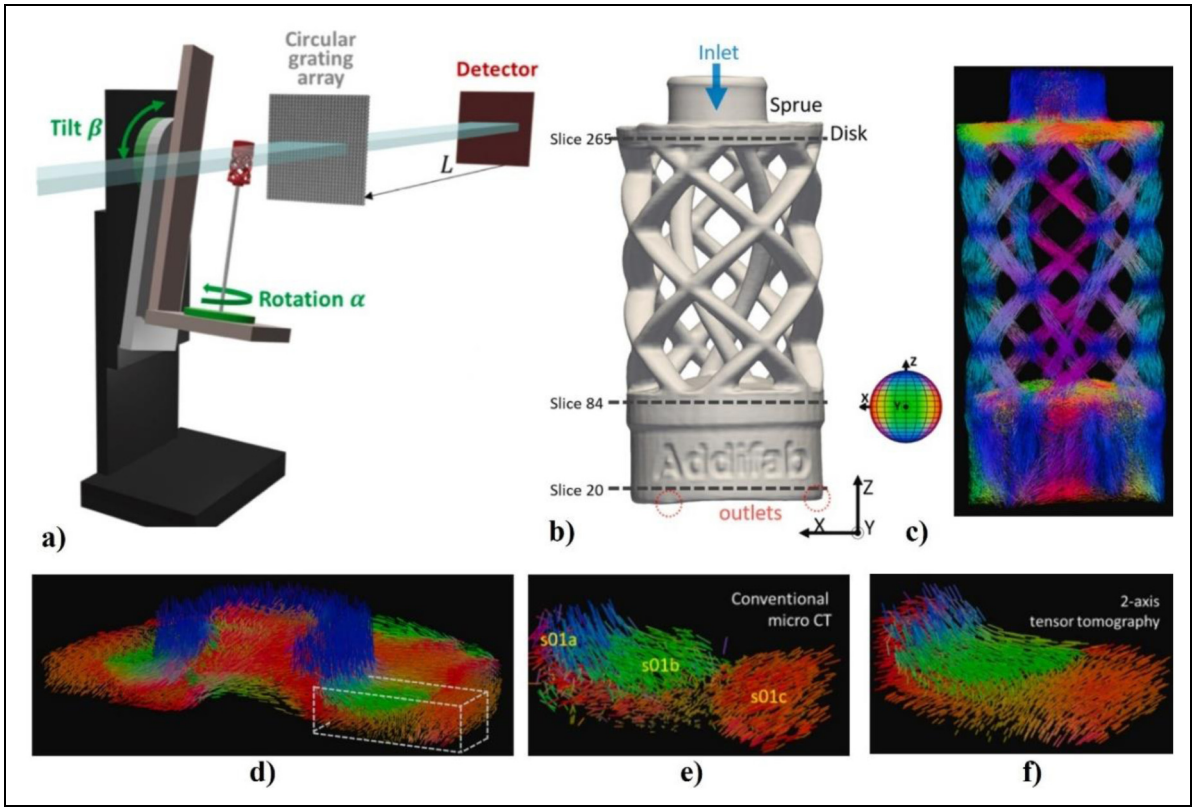

Figure 5. (a) schematic of small-angle X-ray scattering (SAXS) tensor tomography setup, (b) carbon fibre-reinforced freeform injection moulding, (c) preferential orientation of the fibres in each voxel, (d) 3D tensor tomography view around the inlet sprue region with the dashed box showing the location of the magnified region of interest acquired by (e) conventional X-CT image showing the orientation of the actual fibres and (f) tensor tomography showing the inferred orientations.[34]

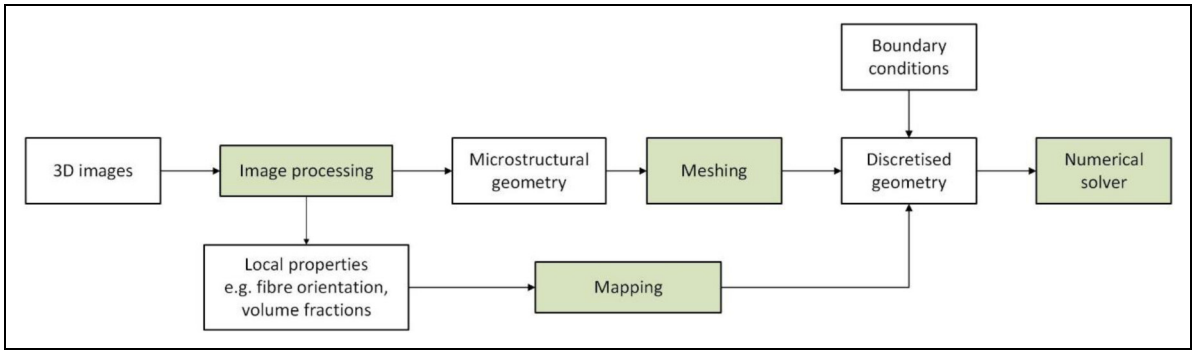

Figure 6. Typical workflow for image-based simulation. The green boxes indicate the processing steps that may involve dedicated development for different material systems.

the structural scale of interest, but not so big that the calculation is computationally infeasible. A lot of research has been undertaken to determine how big the RVE should be.[36,37] In this respect the definition proposed by Drugan and Willis[38] is helpful: ''*It is the smallest material volume element of the composite for which the usual spatially constant (overall modulus) macroscopic constitutive representation is a sufficiently accurate model to represent mean constitutive response*''.

In this section, we consider the image processing (sub-section: *Segmenting images into distinct phases*) and meshing and mapping (sub-section: *Turning phases into finite element meshes*) that are key elements of the image-based modelling workflow shown in Figure 6 before going on to look at the assignment of properties to the constituents in section: *Constitutive equations*.

Segmenting images into distinct phases

A key aspect when using image-based data is the need to assign (or segment) different regions of the images to specific phases or features e.g., matrix, voids/pores and yarns/fibres. This can be achieved through a number of approaches under the broad theme of segmentation. The simplest and still the most widely used method, global

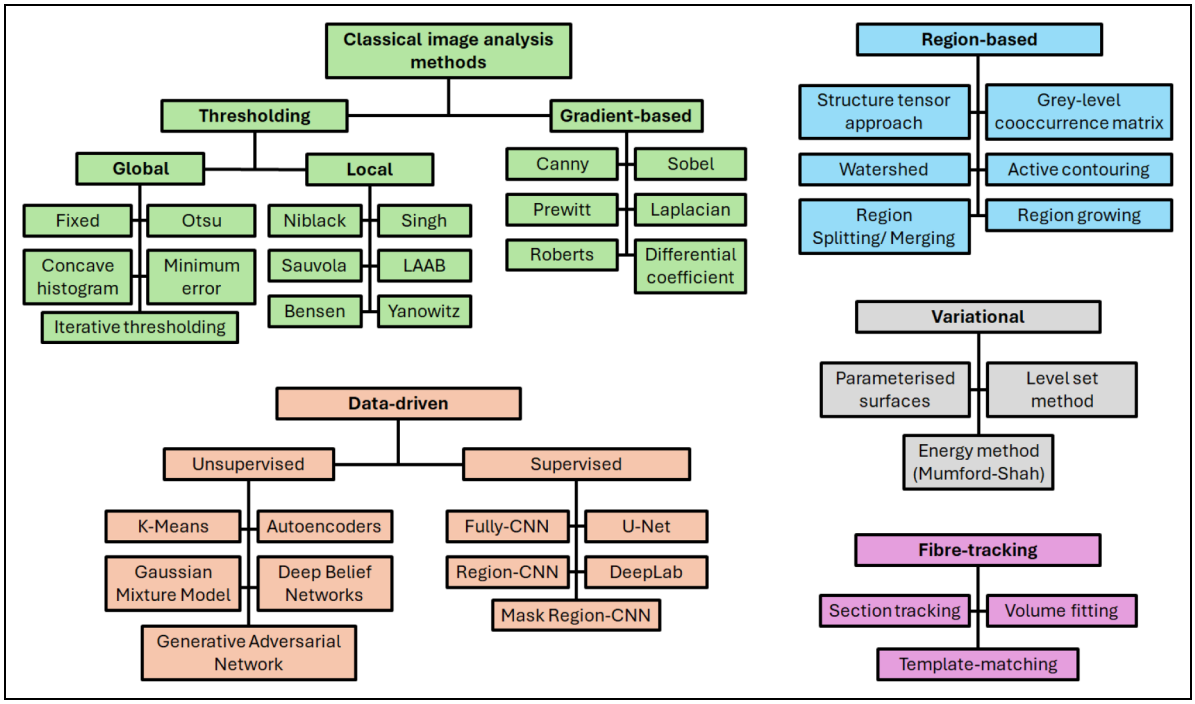

Figure 7. Types of image segmentation methods.[40–43]

Table 1. Advantages and limitations of the various image segmentation techniques (colour coded according to the classifications used in figure 7).

Segmentation category	Methods and techniques	Output	Advantages	Limitations
Classic (intensity/ gradient-based) methods	Global/Local thresholding, Edge detection (e.g., Canny or Sobel).	X-CT image split pixel-wise into phases.	Simple, fast.	Sensitive to noise, variable illumination, poor contrast and overlapping intensity values.
Region-based methods	Region growth, watershed, Grey Level Co-occurrence Matrix, Structure Tensor.	X-CT image split pixel-wise into phases.	Captures spatial continuity of well-defined phases.	May struggle with poor contrast images, does not detect boundaries between different entities of the same phase.
Variational methods	Parametric description of geometry, signed distance combined with level set method, active contouring.	Smooth explicit or implicit surfaces representing phases.	Incorporates prior knowledge of geometry, geometry can be modified using logical operations, smooth boundaries.	Sensitive to initial parameters, may require post-processing to remove overlaps between surfaces.
Data-driven methods	Clustering e.g., K-means algorithm, Machine Learning e.g., CNNs.	X-CT image split pixel-wise into phases.	Captures diverse range of patterns in images, easily adaptable to images of different composites.	ML methods require a large set of labelled images.
Fibre-tracking methods	Tractography, template matching.	3D trajectories of centrelines of fibres/yarns.	Provides continuous geometry of large fibre bundles.	Requires high resolution.

thresholding, is to assign pixels to different phases according to specific greyscale ranges. This method is prone to noise in the image, changes in illumination across the image volume or between different X-CT scans and it cannot accurately segment objects or regions that have overlapping intensity values. Various more sophisticated segmentation approaches have been developed,[39–41] as shown in Figure 7 and Table 1. We classify them into the following categories: classical approaches based on intensity and gradient such as thresholding and edge detection algorithms, region- and feature-based algorithms, variational and model-based methods, data-driven methods and fibre tracking methods. Often, a complex segmentation problem requires a combination of these methods to achieve satisfactory results. A range of software has been developed for segmentation and meshing of X-CT images of composites: the most widely used of these are listed in Table 2.

Table 2. Software used for segmentation and meshing in IBM workflows.

Software	Segmentation	Meshing	Open source	Ref and Examples	Notes
VoxTex	√	√	X	[44]	Structure tensor approach with K-means clustering
OpenFibreSeg	√	X	√	[42]	Tractography for short fibres composites
Avizo	√	√	X	[45,46]	General purpose package
Structure Tensor for Python	√	X	√	[47]	Structure tensor implementation
Dragonfly	√	X	X	[48,49]	General purpose image-processing package
Volume Graphics	√	√	X	[50–52]	General purpose image-processing package
ImageJ	√	X	√	[53–55]	General purpose image-processing package
GeoDict	√	√	X	[52,56]	General purpose image-processing package with additional solvers
Synopsis Simpleware	√	√	X	[57]	General purpose image-processing package
RootPainter	√	X	√	[58,59]	Deep learning based
Insegt Fibre	√	X	√	[60]	Fibre-tracking methods
PolyTex	X	√	√	[61–63]	Parametric modelling

Classical segmentation approaches. A classical computer vision approach to segmentation is to use thresholding and/or edge detection algorithms.

Thresholding methods assign phases according to the global or local greyscale threshold values – pixels or voxels with intensity higher than the threshold are assigned to the foreground and the rest are assigned to the background. A greyscale histogram of an image typically has two or more peaks. In the global thresholding methods, that are often applied to high contrast 2D images of fibres, the histogram is separated using one or more thresholds, which are selected either manually or using, for example, Otsu's method. Noisy or low contrast images or images with imaging artefacts (such as variability in X-ray illumination and effects of beam hardening) require the use of local or adaptive methods that divide the image into sub-regions and apply a threshold calculated using mean and variance of the image's sub-regions. Greyscale thresholding has conventionally been the method of choice for this purpose.[23] Thresholding methods perform well on tasks such as segmenting large pores in laminates, determining fibre volume fractions or void volume fractions in high-quality high-resolution images,[51,64] measuring parameters in dry fibre textiles[65] or for analysing ply waviness in laminates.[66] However, even for relatively simple tasks such as segmenting voids in a composite, the thresholding method underperforms compared to more advanced methods[67] because the difference in greyscale values of voxels are typically not sufficiently distinctive to segment complex X-CT images, and other methods need to be employed.

Edge based methods detect the abrupt changes in intensity of the pixels in the image and use them to mark the boundaries of the objects. These methods are based on classical edge detection algorithms for image processing such as Canny edge and Sobel operators, which apply a series of convolution operators to the greyscale images. Combined with a thresholding algorithm, this is often used for detecting distinct features e.g., fibres in high-contrast images of composites[68], but this approach can struggle to segment X-CT images of complex geometries, such as woven composites.

Region-based methods. This class of methods aims to divide an image into regions based on similarity criteria, such as texture or local fibre orientation, by grouping pixels into regions based on their similarity and then merging or splitting regions until the desired level of segmentation is achieved. One such method is watershed, a classical computer vision algorithm that splits the regions using gradient of the image to construct edges between the regions, which is still used in conjunction with more advanced techniques.

One other method is the grey level co-occurrence matrix, a statistical method which counts frequency of pairs of pixels with given intensities and spatial positions appearing in an image. The homogeneity metric, which can be easily derived from the grey level co-occurrence matrix, can be used to separate yarns in a dry fibre textile[69] but may struggle when applied to carbon fibre composites having a high fibre volume fraction (>55%) because of the poor contrast between phases.[53]

Segmentation of textiles and laminates can also be performed using local fibre orientations (for example using the structure tensor method – see sub-section: *Mechanical models for elements and interfaces*). Typically, the distribution of local orientations obtained using the structure tensor is clustered around the "as-designed" fibre orientations in a composite. Similar to the grey level co-occurrence matrix, segmentation based on these orientations results in a good quality segmentation in case of dry textiles[70] and UD laminates but may struggle segmenting closely packed yarns in textile composites unless combined with variational methods.[71,72]

Variational methods. In many cases of IBM, some parameters of the geometry are already known e.g., principal fibre orientations or structure of a textile. This prior knowledge can be used to create a parameterised or implicit model of the composite geometry that then can be fitted to the X-CT-image using e.g., energy minimisation methods.

Many of the implementations of variational methods require some user input in the form of yarn centroids or yarn outlines.[61,72,73] The input is used to seed the parameters of the model that is fitted to the X-CT image. Bénézech et al.[72] optimised a parameterised geometry of yarns in a woven textile against the greyscale image, comparing the similarity in greyscale and local orientation obtained by structure tensor method. The interpenetration between yarns is prevented by

penalising a regularisation term in the minimisation function. Other metrics can also be used for variational optimisation or Kriging of parametric surfaces e.g., point clouds that describe the surface of yarns in a textile,[61,74] pixel intensity,[73] or edges of yarns in selected cross-sections.[53]

This method has been further improved[53] by using a function that allows a mesh representation of yarns to drive the optimisation process. Such variational methods still rely on manual pre-processing of the 3D image which can be time-consuming. However, these methods offer the advantages of precise representation of the realistic mesostructures even in low-resolution and noisy images (as demonstrated in[48]), and the ability to segment individual yarns (instance segmentation) even when they are touching each other, which is difficult to achieve for example when using the structure tensor method.

An advantage of using parametric or implicit surfaces is that they allow easier manipulations of the surfaces such as Boolean operations, additional smoothing, shrinking of yarns to create gaps between them, or resampling of the geometry independently of the original X-CT image resolution. However, generating implicit surfaces may result in the overlap between these surfaces requiring additional post-processing by e.g., level-set methods or other methods.[67]

Data-driven methods. Generally, data-driven methods may include any method that requires statistical analysis of data. This includes classical clustering methods as well as machine learning algorithms such as convolutional neural networks (CNN). Clustering methods, such as the K-means algorithm, which groups data points based on their proximity to the centre of a cluster, have shown their efficiency in analysing distributions of local fibre orientations to discern warp and weft yarns in X-CT images of textiles.[75]

Machine learning methods can be divided into semantic codes which involves classifying and labelling individual pixels based on their 'semantic' meaning (e.g., groups all fibres) and 'instance' segmentation which involves identifying and outlining individual objects at the pixel level (e.g., a fibre). They can be supervised,[76] where the algorithm "learns" from the training data set by iteratively making predictions on the data and adjusting for the correct answer, or unsupervised,[77] where they work on their own to discover the inherent structure of unlabelled data. While supervised learning models tend to be more accurate than unsupervised learning models, they require upfront human intervention to label the data appropriately. New variants are emerging at pace, such as FCN, U-Net, DeepLab, UNet++, TransUNet, Swin-Unet, and Segment Anything Model (SAM),[78] driven in large part by the medical imaging sector.

Deep learning techniques are increasingly being applied to segment microscale features (fibres, matrix, interphase and pores) for example in a SiC/SiC composite.[79] By training a U-Net with manually labelled 2D images, the authors demonstrated a segmentation accuracy that could not be achieved using classical segmentation techniques, due to the low contrast between fibres and matrix. Sinchuk et al.[48] showed that their Convolutional Neural Network (CNN) model was able to accurately segment features, such as yarns and voids, of a plain weave CFRP from low-resolution low-contrast noisy X-CT images. Blusseau et al.[80] used two U-Nets to track the centrelines and the cross sections of yarns, respectively, to segment an X-CT image of a textile composite. Individual yarns were then segmented through a watershed transform of the distance function map of yarns with yarn centres as markers. This approach only requires the manual selection of yarn centres, which is easier to obtain than the selection of yarn envelopes, facilitating the preparation of the training data to some extent. However, as a supervised learning approach, CNN models still require a considerable number of annotated datasets. This has been offset by including virtually generated data in the training dataset, see e.g.,[81,82]. In,[82] label images with individual yarns labelled differently were obtained from physics-based compaction simulations, then a U-Net model was trained to map these 'instance' segmented images to greyscale images, mimicking the X-CT images. Using the synthetic images, the authors then employed the Mask-RCNN model for the instance segmentation of yarns.

Fibre-tracking (tractography). Similar to model-based and variational approaches, a prior knowledge of the geometry can be used to track long cylindrical fibres in X-CT images. Slice-by-slice approaches are popular and involve detecting the centres of individual fibres at different cross-sectional slices, then linking the fibre centres to form 3D representations of the fibre centrelines (trajectories). This approach is adopted by the 'Insegt' open-source code which has been used to study micro buckling under uniaxial compression.[83] Czabaj et al.[84] proposed a template-matching algorithm to determine fibre centroids on every slide and used a Kalman filter to track fibre trajectories in 3D. The accuracy of fibre tracking depends strongly on the image resolution. Typically, it requires at least 6 pixels[85] across each fibre which means that a voxel size of 1 μm or better is required for carbon fibres, while the larger and higher contrast glass fibres (9 μm–25 μm in diameter) can be adequately tracked at lower resolution.[84] Probabilistic methods of matching the fibre centroids, e.g.,[86] may allow using lower resolution images. Automatic fibre tracking may lead to some erroneous results such as missing fibre sections or incorrect fibre shapes, which requires additional post-processing, as shown in Figure 8. Commercial packages now tend to include fibre tracking analyses as standard. Digital image correlation algorithms have also been used to track individual fibres across cross-sections of a carbon fibre reinforced ceramic composite, either on physical serial slices[87] or those extracted from X-ray tomograms.[88]

Turning phases into finite element meshes

Meshing workflow. Discretisation for a geometry is closely linked to the numerical solver employed in the workflow. For instance, Finite Element (FEM) and Finite Volume Method (FVM) solvers, which are among the most widely used numerical methods in the engineering community, require a discretisation with nodes and elements (subdomains formed by interconnected nodes). Other solvers, such as FFT-based and Finite Difference Method solvers, only require a regular grid. For such cases, image discretisation can be performed at either the initial resolution or after down-sampling (i.e., reducing the resolution by grouping pixels or voxels), which significantly simplifies the meshing

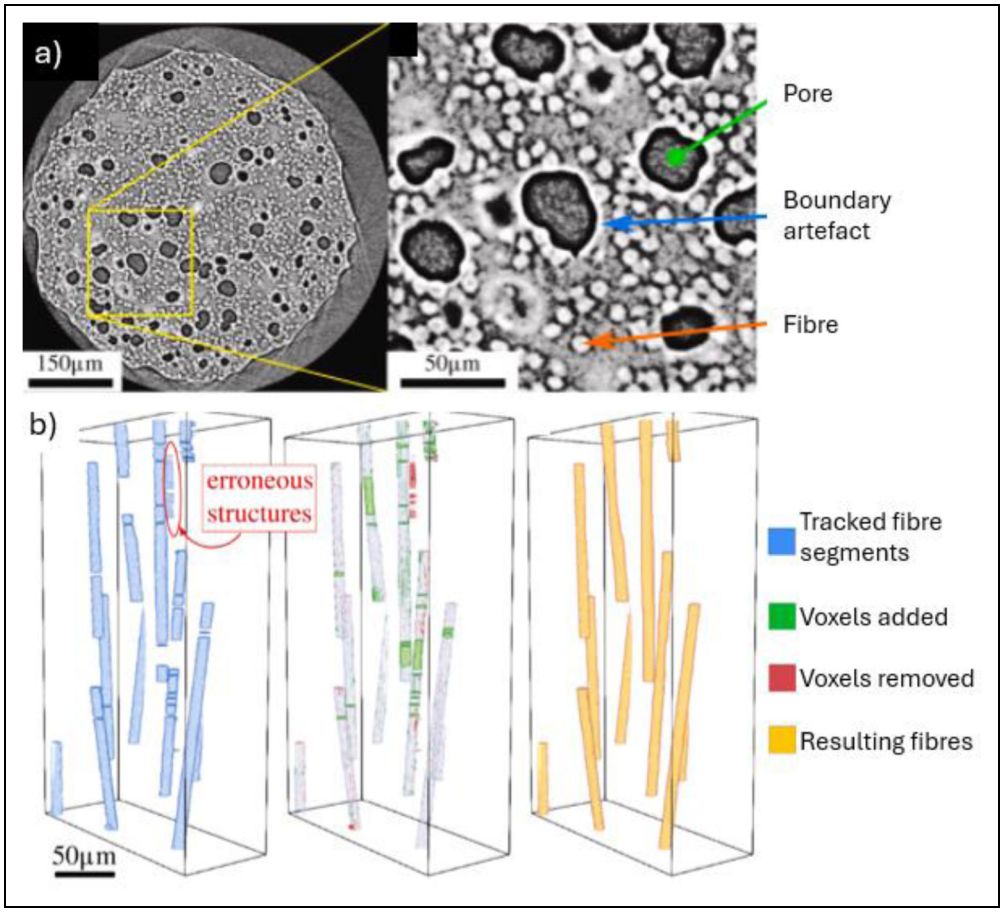

Figure 8. (a) sample 2D slice of tomographic scan of a PEEK 40 wt.% CF filament (after histogram equalisation), and (b) post-processing showing (left) fibre segments from the fibre tracking analysis, (centre)) morphological closing to add missing (green) segments and to remove a few erroneous (red) features and (right) the resulting fibre volumes.[42]

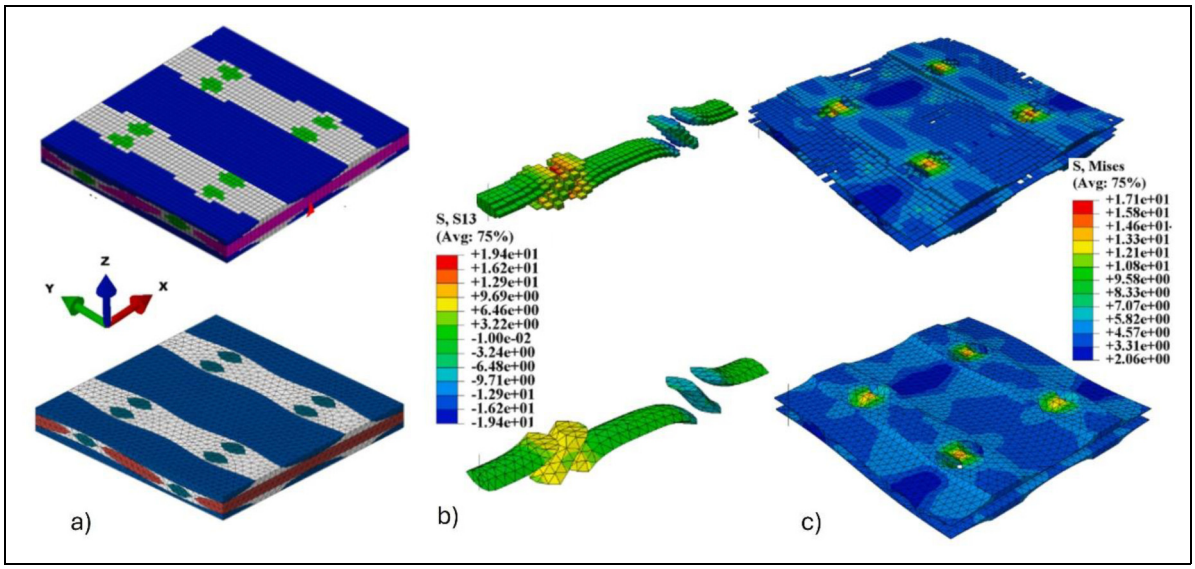

Figure 9. Voxel (top) and conformal (bottom) RVE representations of a 3D woven composite subjected to warp tensile loading showing (a) the meshes, (b) shear stress in one of the binder yarns, (c) comparison of von Mises stress fields.[90]

process. Meshless solvers, such as the Discrete Element Method, Smoothed Particle Hydrodynamics and peridynamics are available in the computational mechanics community, but applications in image-based simulation are not yet popular, possibly due to their limitation in accuracy of stress/strain predictions and the lack of standard software packages. Producing high quality FEM meshes of the complex 3D geometries typical of textile composites remains a challenge, as discussed elsewhere.[89] FE meshes for composites are generally classified into two

categories: conformal and non-conformal (voxel) meshes. The difference between these two types of meshes lies in how they represent the boundaries between the phases as illustrated in Figure 9. Obtaining a conformal mesh is typically more desirable, but more difficult, than generating a voxel mesh.

The nature of X-CT images lends them to **non-conformal voxel discretisation** (voxel mesh), which is equivalent to the X-CT image is generated, with each voxel assigned to different phases based on the segmentation process. Although, the resulting voxel mesh can be used "as-is",[91,92] the "jagged" interfaces (Figure 9(a), top row) often lead to unrealistic predictions of local stresses during structural analysis[93] (Figure 9(b) and (c)). This issue is typically mitigated by post-processing of the voxel mesh. This includes reassigning voxels from one phase to another e.g., isolated voxels or thin layers of voxels belonging to yarns may be reassigned to the matrix in a mesh of a textile composite.[93,94] The second technique is applying smoothing to the nodes along the interfaces between different phases.[93–95] It should be noted, that since the voxel meshes are derived directly from X-CT images, they can be computationally inefficient due to the uniform element size, which may be unnecessarily small in areas where high resolution is not required. Various methods, such as octree-based mesh refinement and coarsening,[95] are used to reduce the mesh size yet keeping the accuracy of the simulations.

Conformal meshes represent the phase interface more accurately (Figure 9(a), bottom row) than voxel meshes (Figure 9(a), top row) and are therefore often preferred to obtain high-fidelity predictions. However, generating a high-quality conformal mesh, i.e., a mesh with average Jacobian ratio of 1, can be challenging. This is particularly the case when an X-CT image contains several phases with complex geometries in close contact, such as closely packed UD fibre bundles and textile composites.

The generation of a conformal mesh begins with post-processing of a segmented X-CT image. Initially, surfaces of the phases need to be generated. This can be done by extracting interfaces directly from a voxel mesh of the segmented X-CT image and applying an explicit smoothing algorithm e.g., Laplacian smoothing[94,96] directly on these surfaces or those constructed using marching cubes algorithm from the voxel mesh.[97] Alternatively, implicit surfaces may be constructed by defining a signed distance function for each phase (e.g., fibres or yarns) and employing a level-set method to determine their boundaries. The resulting boundaries then can be smoothed using Gaussian filter ("blur") to remove irregularities that Laplacian smoothing is unable to eliminate.[67]

Once the surface meshes have been obtained, it is possible to generate a volume mesh. Typically, a tetrahedral volume mesh would be created for composites and a mesh consisting of hexagonal or triangular prismatic elements would be generated for models of dry fibre reinforcements[98] or laminates.[66,81,82] An example of a conformal mesh of a textile composite is shown in Figure 9. This example illustrates a mesh that is generated by applying an explicit smoothing to a voxel mesh to obtain surface meshes of the yarns. The surface mesh is then remeshed to improve their quality and the resulting surface meshes are used to generate a tetrahedral volume mesh. In some cases, for example when a macro-scale model of a composite is required, a generation of the mesh can be relatively simple. Seon et al.[99] generated a hexahedral mesh of a composite laminate with local waviness by morphing a rectangular grid mesh to fit segmented X-CT data.

Challenges when generating meshes for composites. Some of the challenges in generating conformal meshes relate to general difficulties of meshing finite element models containing small features such as sliver-like regions between yarns, which require excessively small element size near these features. A common approach to address this issue is to increase the size of the problematic regions to allow for larger element size. In the case of textile composites, this would typically mean introduction of an artificial gap between yarns, which is made feasible by the implicit description of the geometry. However, these adjustments need to ensure that the overall and local fibre volume fractions remain realistic.

Another common difficulty when using X-CT images to build a model of a composite is the question of selecting an RVE of an appropriate size. For numerical simulations at the micro- and meso-scales, it is often desirable to prescribe periodic boundary conditions (PBCs) on the edges of the RVE because PBCs require smaller RVEs to be statistically representative of the homogenised properties.[37,95,100] However, the 2D and 3D images used for image-based modelling are unlikely to have an inherently periodic structure. Some solutions have been developed for this problem such as modifying the geometry of the model to enforce periodicity at micro-[101] or meso-scales,[102] or using modified periodic boundary conditions, such as weakly periodic boundary conditions.[103] In all cases, it is important to remain vigilant because the boundary may not be sufficiently representative of the real microstructures.

Constitutive equations

Mechanical models for elements and interfaces

Once segmented into the constituent regions, the properties representative of each region and their interfaces to other regions must be applied. This can be for specific phases (e.g., matrix, reinforcement, interfaces), but also to 'composite' domains (e.g., yarn, laminae). The former is relatively straightforward; in the latter cases the properties can be determined from a smaller (image-based) sub-model or inferred from a knowledge of the fibre orientation. The orientation of fibres and hence the mechanical properties to be assigned to each finite element can be obtained directly from X-CT if the individual fibres have been tracked (see sub-section: *Segmenting images into distinct phases* and Table 3). In other cases, the average fibre orientation within each element can be determined by SAXS tomography (sub-section:*Small-angle scattering tensor tomography*, or by structure tensor analysis from X-CT images even when the contrast or resolution is not sufficient for the individual fibres to be segmented (see Table 3).

Structure tensor analysis[47,130,142] allows local fibre orientations to be estimated without tracking individual fibres. In the structure tensor method, the principal direction and the

Table 3. Applications of high-fidelity and structure tensor methods to the identification of fibre orientation in fibrous composites.

Method		Type of fibrous reinforcement	References
Sections + tracking	Template matching and multi-target tracking	UD carbon-epoxy bundle	84,104–107
	Pattern dictionary and classification (InSegt)	UD carbon-epoxy bundle	60,108–112
		Random short glass fibres, additive manufacturing	42
	Digital image correlation	UD carbon-epoxy bundle	88
Volume fitting	Cylinder template matching (Avizo)	Random short fibres (glass, basalt, carbon, polyester)	113,114
		Spun cotton yarns	115
		Braided cellulose fibres	116
	Tracking fibre backbone based on structure tensor estimation	Wood short random fibres in PLA	117
Structure tensor	UD bundles	carbon	111,118
		glass	119,120
		flax	44
		steel	121
	Laminates with UD layers	carbon	122–126
		glass	127,128
	Non-crimp fabrics	carbon	129
		glass	30,47,70,130,131
	Woven 2D	carbon	132
		wool	133
		ceramic	134–136
	Woven 3D	carbon	121,137
		glass	89
		ceramic	72,138
	Braids	ceramic	139
	Short random fibres	carbon	30,140,141
		glass	34,142–144
		mineral wool	145
	Long random fibres	carbon	146–149
		glass	150
	Fibres in bio- tissues	collagen	150,151
		synthetic	152

degree of microstructural anisotropy can be calculated from the structure tensor $\boldsymbol{S}'$ of the image $I(x, y, z)$ in terms of

$$\boldsymbol{S}'(x,y,z) = \begin{bmatrix} \left(\frac{\partial I}{\partial x}\right)^2 & \frac{\partial I}{\partial x}\frac{\partial I}{\partial y} & \frac{\partial I}{\partial x}\frac{\partial I}{\partial z} \\ & \left(\frac{\partial I}{\partial y}\right)^2 & \frac{\partial I}{\partial y}\frac{\partial I}{\partial z} \\ sym & & \left(\frac{\partial I}{\partial z}\right)^2 \end{bmatrix} \quad (3)$$

Structure tensor analysis can be undertaken using open-source or commercial software (see Table 1). Using this approach, the degree of local fibre orientation distribution can be inferred for each volume element in a finite element model and the relevant mechanical property tensor assigned.

Once the parameters of the fibrous material in the elements are identified, the anisotropic stiffness matrix is calculated using micro-mechanical theories,[153–155] and then the homogenised stiffness matrix of the material is calculated. This is performed either using analytical homogenisation methods, such as orientation averaging or Mori-Tanaka,[156] or with FE homogenisation, which involves the solution of six boundary value problems, corresponding to different elementary loading patterns.[157] When assigning the properties to a yarn in a woven or braided material, it is important that the properties are aligned with the fibre orientation direction at each location rather than the overall coordinate directions (e.g., the warp or weft directions).

Image-based models play an important role in modelling inelastic behaviours. For example, the resin matrix of polymer matrix composites (PMCs) is typically modelled with an isotropic elasto-plasticity constitutive law.[158] As a consequence, the behaviour of lamina or fibre yarns at the mesoscale is often described with elastic-plastic models, though anisotropy is required due to fibre orientations. Several studies have demonstrated that incorporating plastic behaviour is crucial for the model to accurately reproduce experimental measurements (see. e.g.,[159,160]).

Damage initiation and propagation criteria

There is a plethora of mechanisms by which damage can occur in composite systems (See Figure 10) and these include:

- **Matrix failure** by cracking or ductile voiding; often the lowest strength component in a composite. The brittle nature of polymer and ceramic matrices mean matrix cracking is the main source of failure in composites and may initiate other modes of failure, such as delamination and debonding.

- **Ply delamination or interlaminar debonding** which is one of the most commonly encountered failure modes in composite laminates.
- **Interfacial debonding and sliding** – while the interface is often taken to be strong for polymer matrix composites, interfacial sliding and pull-out are key toughening mechanisms in long fibre ceramic and metallic matrix composites.
- **Reinforcement fracture** – often the last failure mode leading to significant loss of strength. The fibre failure strength is probably best described by a Weibull strength distribution.[162]

One approach is not to model such microscale damage explicitly (with its heavy computational cost) but to use a continuum damage mechanics (CDM) approach[163] within a FE framework. Here, the accumulation of microscopic damage such as matrix cracks, fibre breakage, and delamination at finer scales can be accounted for indirectly treating the material as a homogeneous continuum instead, allowing for analysis of the overall structural response as damage evolves throughout the material. In certain cases, microscale image-based modelling can be used to develop CDMs at a coarser length scale. CDM requires two material models: one for damage initiation and one for damage evolution. It uses damage parameters to describe the damage in composite constituents which start at zero (no damage) and progress to one (completely damaged). These increase gradually such that damage can progress within an element as well as throughout the mesh. Separate damage initiation criteria can be used to describe matrix, fibre, interfacial and intralaminar failure. The degradation in the mechanical response can be gradual as the damage variable increases or represented by a step-jump. Beyond quasi-static material models, dynamic behaviour, such as impact[164] and fatigue[165] have also been modelled for fibre reinforced composites. However, image-based modelling of these dynamic behaviours is in its infancy. It is anticipated that this will increase as more experimental data from X-CT observations become available.

Crack propagation modelling can be broadly divided into two different strategies: sharp interface and diffuse interface approaches where the crack is smeared over a small but finite length. In the FE modelling, the fracture process is typically modelled across the three constituent phases (fibres, matrix and interfaces) using pre-inserted cohesive interface elements. This has the drawback that it is possible that the locations of the cracking mechanisms are not quite right, which may affect the micro-damage processes and their responses on the global scale model, although adaptive meshing can be used to vary the crack path.[166] Crack growth is allowed to progress through each of the three phases without restriction. Matrix cracking and interfacial debonding behaviour can most simply be modelled by the breaking of cohesive elements using one of two criteria, namely a maximum stress failure criterion, which is based on the highest ratio of the stress to the peak stress in each of the three orthogonal material directions, or a quadratic criterion, which is based on a quadratic combination of all three ratios, with the latter criterion being particularly useful in modelling mixed-mode behaviours.[161]

Much less commonly, meshless methods have been applied. They avoid a predefined fixed connectivity between the nodal points used to define the geometry. As a result of the connection-free nature of the nodal discretisation, any crack propagation paths can be efficiently embedded geometrically within the numerical model. Often, they are used in conjunction with CDM to model damage evolution and crack propagation. Despite the higher accuracy and flexibility, meshless methods tend to be more difficult to master. Of these methods, the extension of FEM into XFEM is gaining traction.[167] It retains some advantages of the FEM but allows the singular stress state at a crack tip to be reproduced while allowing multiple cracks or arbitrary crack propagation paths to be simulated on an independent unaltered mesh. Critically the mesh does not need to conform to the virtual crack path.

Modelling/simulation

Here we consider IBM at specific scales (sub-section: *Modelling at specific scales*) before looking at multiscale modelling (sub-section: *Multiscale modelling*). Figure 11 summarises the way information flows between these scales. It is worth noting that the output from microscale modelling can be used to develop the constitutive relations for yarns/tows for those composites having mesoscale features, such as 2D woven composite materials. Theseoutputs can also be directly used as inputs for macroscopic modelling of composites without mesoscale features, such as unidirectional composites. In this respect, the key issues limiting the application of IBM are chiefly image resolution and segmentation. Resolution is a double-edged sword, in that for IBM, higher resolution imaging is not necessarily better; rather, it depends on the specific scale of the analysis and objectives. For high-resolution images, extensive microscale surface waviness can trouble FE mesh quality, as well as giving difficulties in segmenting individual fibres in microscale models.

Modelling at specific scales

Microscale models: The most common challenge for image-based modelling at the microscale is related to limitations in terms of image resolution and contrast. X-CT images of composites commonly feature voxel sizes around 1 μm, which should be compared to typical fibre diameters: e.g., 5–7 μm for carbon fibre, 9–20 μm for glass fibres and 140 μm for SiC monofilaments. For laboratory scanners, this can result in difficulties in resolving fibres accurately.[168,169] Significantly better image quality can be obtained using synchrotron sources, but this does not fully resolve the image quality concerns (see for example the low contrast of carbon fibres in Figure 4(b)). Lower-quality segmentations are manageable in terms of elastic properties but are often problematic for modelling damage development and fracture. The typical complications for microscale modelling include:

- Modelling interfacial debonding through cohesive surfaces or elements requires that the segmentation process creates surfaces which are ideally relatively smooth. Sub-section: *Segmenting images into distinct phases* has identified strategies that can help to achieve this.

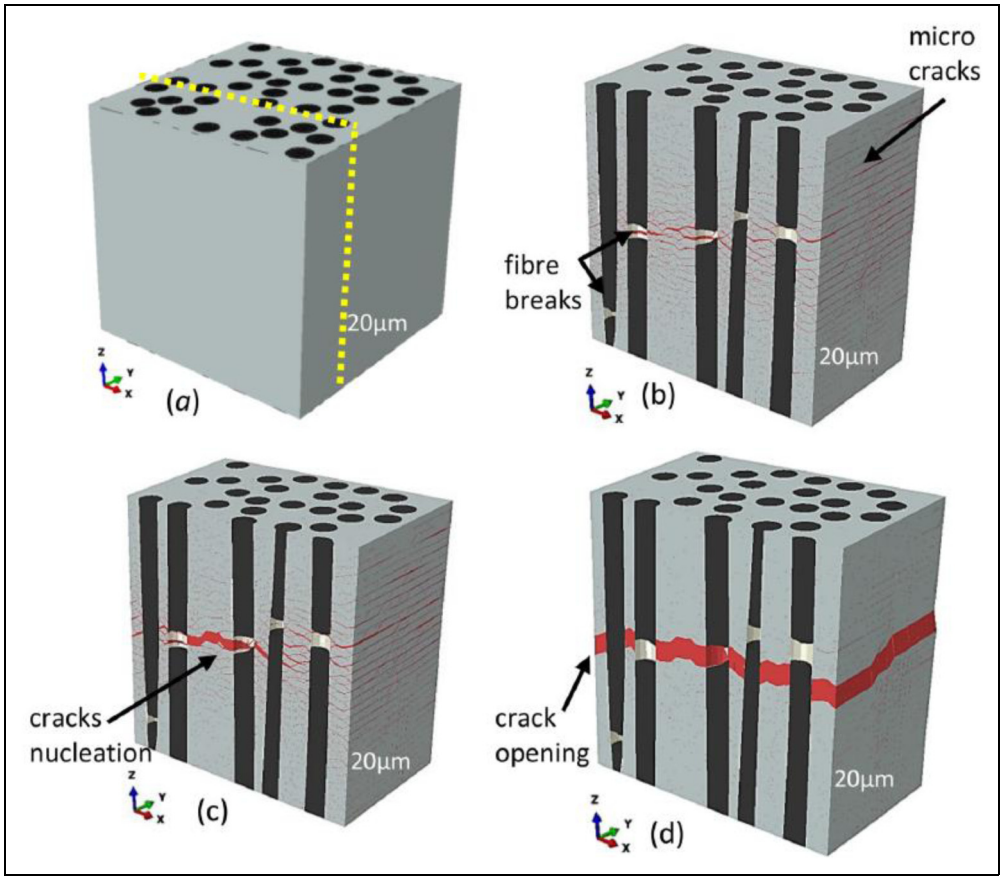

Figure 10. Sequence of microscale damage and crack propagation for a ply of a double notched $(-45°/90°/+45°/0°/-45°/90°/+45°/0°)_s$ carbon fibre epoxy composite sample under progressively increasing tension along the fibre-axis (z) using a phase-field regularised cohesive zone model (PF-CZM) with softening laws.[161]

- Fibres may be straight at the scale considered, but segmentation errors often lead to slight misalignments or waviness due to noise. These errors can be critical in predicting some microstructurally sensitive properties, such as compressive strength.
- Meshing is often difficult when fibres are very close to each other, leading to poor mesh quality and convergence issues due to distortions. Nevertheless, these high local fibre volume fraction regions are crucial in predicting damage development, failure and permeability.[170] The embedded elements method may help resolve meshing issues, but it does create volume redundancy concerns and the combination with cohesive zone modelling (CZM) is not straightforward.[171,172]
- Microscale models also need accurate information on the fibre orientation,[168] meaning that simply meshing segmented images is insufficient. Often this is needed at the individual fibre scale rather than the fibre bundle scale which means that high-fidelity methods can be more appropriate than structure tensor methods (see Table 3).

Mesoscale modelling: Mesoscale models generally relate to textile composites (such as 2D and 3D weaves or braids), fibrous and ceramic laminates and filament-wound structures. Issues with textile composites relating to voxel and conformal meshing have been discussed in sub-section: *Turning phases into finite element meshes*. In many cases, their periodic nature means that RVE methods can be appropriate.

Macroscale/component modelling: Image-based macroscale models offer a computationally efficient approach to numerical analysis by representing the micro- and mesoscopic features (e.g., fibres/tows, interfaces, and matrix) as homogenised macroscopic materials (albeit with anisotropic properties). This simplification facilitates the rapid computation of mechanical responses and promotes broader engineering applications. However, a critical challenge lies in deriving accurate macroscale constitutive inputs for homogenised macroscale materials, which significantly influence the precision of the macroscopic equivalent models. Methods such as multiscale modelling[161] and experimental testing[173] have been employed to address this issue, though a unified theoretical framework for composites with diverse structural configurations remains elusive. Additionally, high-resolution imaging[8] plays an important role by providing detailed boundary definitions that capture the actual macroscale material geometry based on the segmented models. However, segmentation errors frequently undermine the modelling process, complicating the analysis of damage initiation and propagation. The challenges in macroscale modelling include:

- Surface imperfections, such as pits or bumps extending over tens of micrometres, impose constraints on FEM by limiting the element size. This significantly increases computational demands and complicates numerical damage simulation. High-resolution imaging, typically

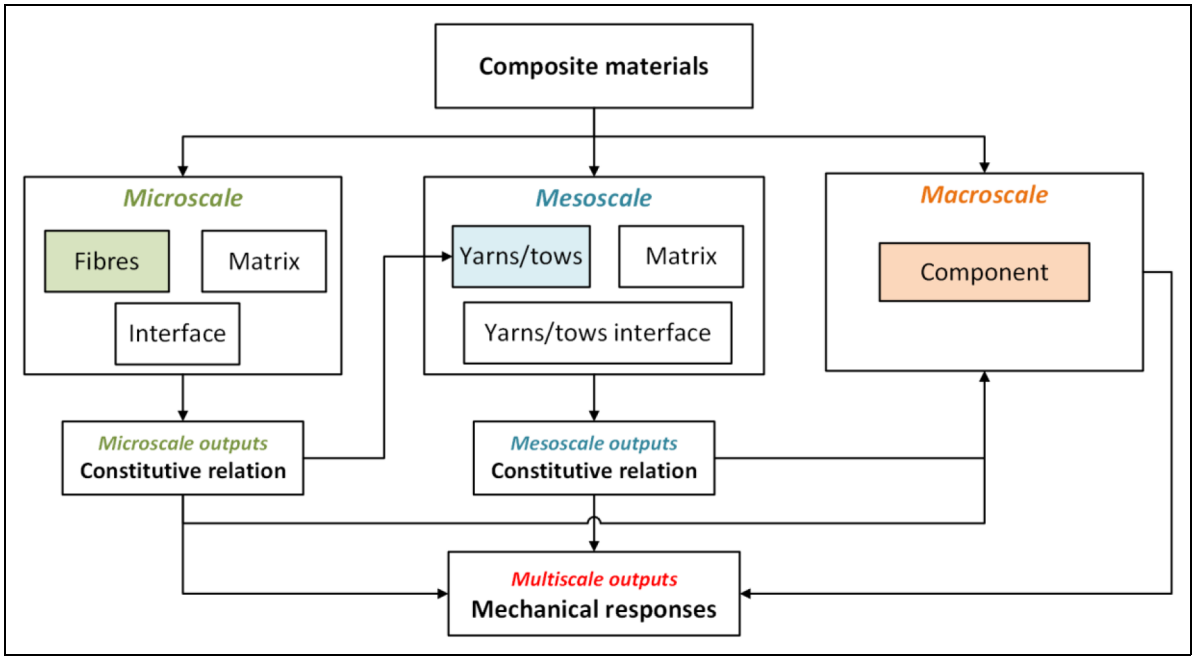

Figure 11. Strategies for composite modelling at different scales.

achieved through lab-based X-CT at 4–8 μm resolution,[21] can provide detailed and accurate information about surface flatness, which may include many surface imperfections at the micrometre level.

- Material defects, such as porosity and cracks, will often need to be considered in macroscale image-based modelling.
- Typically, most synchrotron scanners have fields of view at the centimetre scale, although a notable exception is the BM18 beamline at the European Synchrotron Radiation Facility. Consequently, whole component scanning is usually undertaken using lab X-CT scanners.
- Many composite components are essentially flat panels which are not easy to scan in conventional scanners. In some cases, laminography[174] can be used to overcome this issue.
- If the lower-scale model is RVE-based, then it can be difficult to pass on damage-related information because most homogenisation methods often focus on the elastic properties. This inherently limits the accuracy of macroscale models. This issue and potential solutions are discussed in more detail in sub-section: *Multiscale modelling*.

Multiscale modelling

Although image-based methods are often appropriate at specific scales (micro, meso, macro), one often needs to link the image-based and continuum-based models in a multiscale manner, where the effective behaviour of the upper scale is derived from averaging the behaviour at lower scales. Numerical homogenisation is a well-established technique for composites,[175] at least when the length scales are well separated, and one can determine a periodic RVE. A clear separation of scales between the meso- and the macroscales can break down where the size of the heterogeneities at the mesoscale is comparable to that of the sample. Also, determining a proper RVE[37,176] for complex composite structures[177] can be challenging as the underlying microstructure changes continuously within the specimen. This difficulty is exacerbated in image-based approaches that account for both geometric[178–181] and material variabilities,[182–184] resulting in fully stochastic models. Direct simulation of large-scale specimens, while resolving all the microstructural details demands the use of high-performance parallel computing and dedicated domain decomposition methods[185,186] with specialised preconditioning techniques.[187,188]

Alternative, more computationally efficient, strategies have been proposed by constructing an approximate heterogeneous macroscale model where the underlying microstructure is not fully resolved, but is still taken into account. One may, for example, filter the underlying (micro-/meso-scale) heterogeneities,[189] or perform only local homogenisation to determine varying apparent properties[138,190–194] at a scale compatible with the computation at hand. These approaches could be extended into the framework of multiscale FEM[195,196] by projecting or condensing concurrent solutions at a lower scale onto the computational mesh.[197,198] Finally, global-local approaches[199] allow the coupling effort to focus only on regions of interest where a fine description of the lower scale is required. However, ensuring the continuity between the local and global models, especially when strong heterogeneity crosses the interface, remains a significant challenge.[200,201]

Surrogate modelling[202,203] serves as a mathematical approximation technique that replaces high-fidelity simulations or experiments by learning the input-output relationships from existing data. It is widely used to accelerate complex analysis and optimization tasks by significantly reducing computational cost while maintaining acceptable predictive accuracy. This is particularly important in progressive damage simulations, where finite element (FE) analyses involve severe geometric and material nonlinearities and

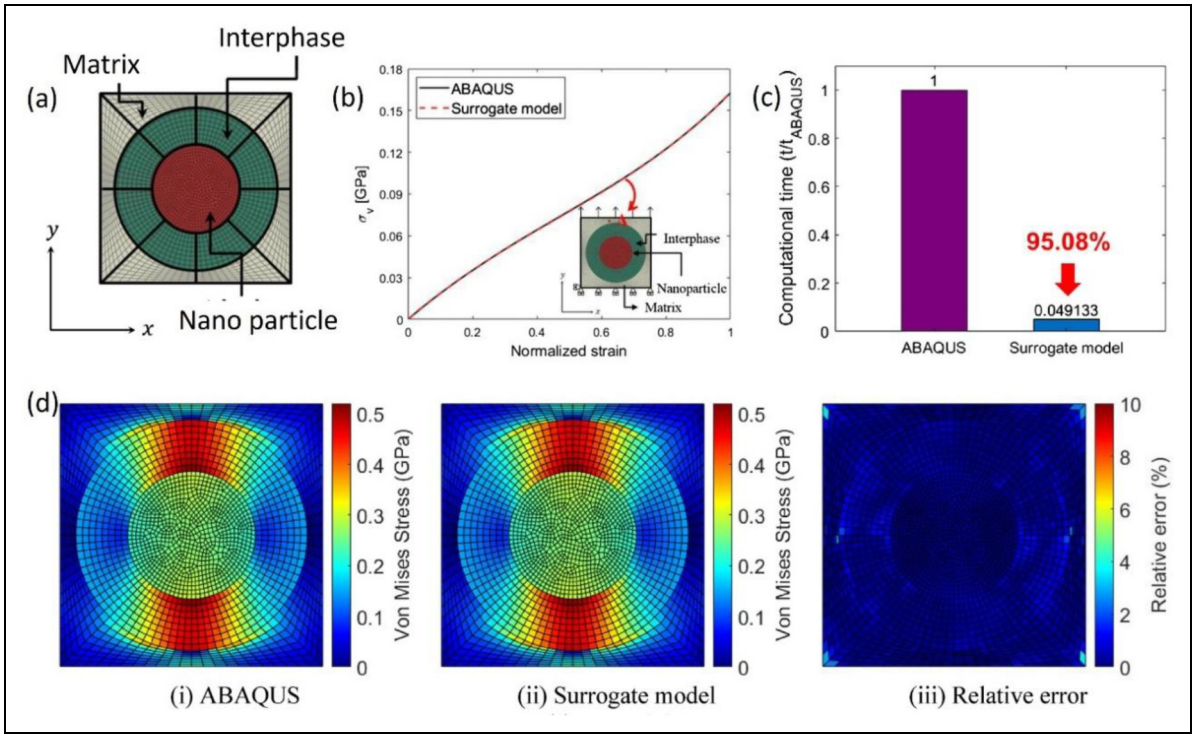

Figure 12. Surrogate modelling of nanocomposites. (a) unit cell for the nanocomposite (FE model), (b) macroscopic stress-strain response and (d) microscopic stress field comparison of the surrogate and FE models, comparison of (c) the computational time and (d) the von Mises stress fields associated with the surrogate and FE models.[208]

demand intensive computational resources. Various surrogate modelling strategies have been developed to suit different simulation scales, each with distinct assumptions and trade-offs. Among the most widely adopted approaches are Gaussian Process Regression (GPR), Reduced-Order Modelling (ROM), and Artificial Neural Networks (ANNs). GPR is a kernel-based Bayesian regression technique that offers high predictive accuracy along with uncertainty quantification, making it especially effective in small-data scenarios - though it comes with considerable computational expense.[204] ROM reduces the dimensionality of high-fidelity models by projecting them onto a low-dimensional subspace, enabling fast predictions at the cost of reduced accuracy in highly nonlinear regimes.[205] ANNs, loosely inspired by the architecture of the human brain, are capable of capturing complex nonlinear patterns from large datasets, but they often require extensive training data and suffer from limited interpretability.[202,206–208]

Given the varying requirements across scales, surrogate modelling approaches should be tailored accordingly. At the microscale, where capturing fine-grained nonlinear behaviour is essential, high-accuracy methods such as GPR are typically preferred. At the mesoscale, a balance between accuracy and computational efficiency is often sought, making both GPR and ANNs viable options. At the macroscale, the focus shifts primarily to computational speed, favouring surrogate strategies like ROM and ANNs. Despite their growing adoption, surrogate models still face several challenges, most notably the lack of integrated multiscale surrogate frameworks that can seamlessly bridge different physical scales within a unified modelling architecture. However, the developing ANNs, which demonstrate superior cross-scale modelling capabilities, offer valuable insights into the development of multiscale surrogate modelling strategies. For example, Kim et al.[208] developed a deep learning driven surrogate model for a nanocomposite (see Figure 12) to investigate its inelastic behaviour of microstructure. The surrogate model was able to mimic both the macroscopic stress strain response and the microscopic strain field with a dramatic decrease in computation time.

Applications

It is not possible in this review to cover all the applications of image-based modelling undertaken so far; rather the following sections are illustrative of the applications that can be served by such approaches and the aspects that need to be considered when doing so. Many of the examples are taken from the polymer composites area, but the approaches can easily be applied to other composite systems.

Composite manufacturing

Many polymer, metal and even ceramic matrix composites are formed by infiltrating the dispersed reinforcement (often in the form of a textile or fibre preform) with a fluid (e.g., liquid resin, slurry or molten metal). In all cases, the aim is to produce a fully dense composite in the shortest possible time. In the case of metal matrix composites, the temperature and time at temperature are often minimised to prevent interfacial reaction. In polymer infiltration pyrolysis (PIP) of ceramic matrix composites, the number of infiltration steps is of concern, while in polymer infiltration of polymer matrix composites, air entrapment and fibre-free/resin-rich areas are of interest. As a result, X-ray imaging is being increasingly

used to study the infiltration processes aided by simulations used to design and optimise the infiltration processes.[209]

Changes in the reinforcement distribution can occur during processing, either compacting and thereby closing pore channels, or separating them to create reinforcement-free regions.[210] To capture this, Yousaf et al.[46] have used the digital element approach[211] to model how nesting and compaction of carbon fibre textiles can reduce the pore spaces and, thereby, the changes in permeability as the pore channels close with increasing pressure.[45] In other cases, textile reinforcements (dry or prepreg) are deliberately deformed into a desired 3D shape (i.e., draped) onto a mould. In such cases, X-CT can be used to help develop mesoscale simulations that incorporate the typical modes of textile deformation – shear, biaxial tension, and compaction.[212]

With regard to liquid composite moulding processes, a great deal of work has been undertaken using image-based modelling to predict the permeability of fibrous networks. These approaches have considered both the mesoscopic pore channels between tows and the microscopic channels within them. In this respect, a round-robin study (international Virtual Permeability Benchmark)[170] has evaluated the state-of-the-art of existing numerical approaches for microscale permeability prediction by considering a single fibre bundle region of interest (400 fibres wide and having a length of ~500 μm) that had been extracted from an X-CT scan of a twill-weave fibre glass-reinforced composite. The round-robin study concluded that the predictions of axial permeability showed less scatter (presumably because of the simpler flow paths) than the transverse permeability and also that for microstructures with unknown principal directions, or with anisotropic effects, applying symmetric or no-slip boundary conditions was not appropriate and a method that determines the full permeability tensor is needed. The permeability of such microstructurally realistic models can then be used as an input for mesoscale calculations of flow through the fabric to deduce its macroscopic permeability. This was the topic of the second phase of this round-robin on the image-based permeability prediction,[213] which highlighted the need to take great care in selecting an image with a mesostructurally representative RVE, which may or may not contain continuous inter-tow flow paths that dominate the intra-tow flow.

With regard to woven fibre composites, Ali et al.[56] found that for a 3D angle interlock carbon fibre composite the percentage of areal gaps in the warp direction were less than in the other two directions, but that these were reduced less than for the other two directions upon compaction. The flow channels for flow in the weft direction are shown in Figure 13(a). Similar approaches would also be appropriate for ceramic processing by PIP, where the situation is complicated by the fact that the channels reduce in size and connectivity each PIP cycle as full densification is approached.

Image-based infiltration studies have also been undertaken for particulate composites. For example, Guo et al.[214] used a pore-scale, non-isothermal two-phase flow numerical model to describe the infiltration of liquid Al metal into a SiC porous preform. They found that the infiltration pattern transitions from stable displacement to capillary fingering due to changes in the local meniscus dynamics, and that void trapping stability is

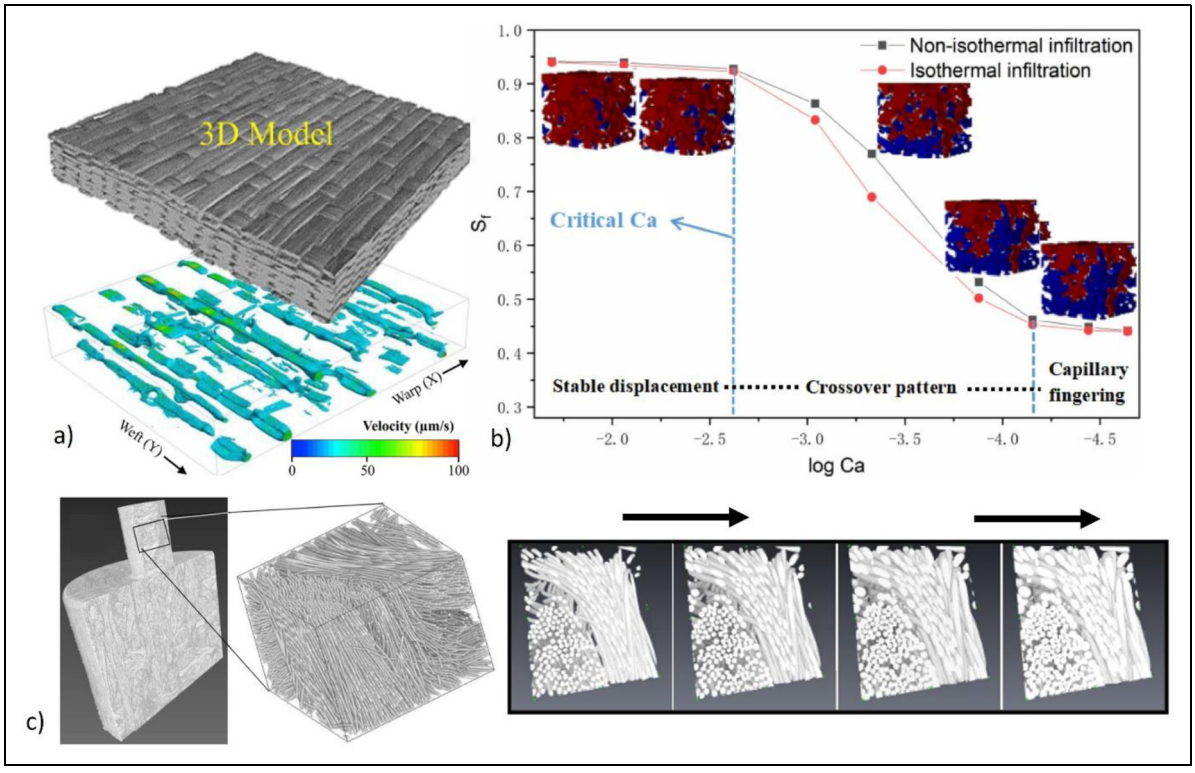

Figure 13. Examples of infiltration modelling. (a) X-CT image-based model for a 3D angle interlock carbon fibre fabric (top) and resin flow fields (bottom) showing flow paths in the weft direction,[56] (b) predicted flow of liquid Al metal through an IBM of porous SiC showing the steady-state fluid saturation, S_f, with respect to capillary number, Ca. The insets show the non-isothermal distribution of fluid (red) in the SiC (blue),[214] (c) time-lapse sequence showing a micro-scale pore chemical vapour infiltration simulation based on a 3D image of a C-fibre preform from an X-CT scan (left).[215]

higher in the capillary fingering pattern (see Figure 13(b)). As a result, there is a critical capillary number (Ca) value, above which the local macroscopic void concentration can be avoided.

CMCs such a C/C composites are often produced by chemical vapour infiltration (CVI) involving the infiltration of a heated fibrous preform by the chemical cracking of a vapour precursor. The density of materials prepared by CVI relies on processing conditions and the microstructure of the preform. Similar image-based methods to those described above can be used, but with gas transport modelled rather than liquid transport. In Figure 13(c), a random-walk-based infiltration framework has been applied for the fibre-scale modelling of chemical vapour infiltration of a carbon fibre preform.[215,216]

Elastic properties

One of the primary applications of image-based modelling in composite materials is predicting elastic properties. Studies leveraging advanced imaging techniques, such as micro-CT and X-ray scattering tensor tomography,[30–35] have enabled researchers to extract detailed information about the effect of fibre orientations, volume fractions, and local microstructures of composites, which can both elucidate the knock-down associated with imperfect fibre/yarn alignment and manufacturing defects, as well as point the way to improved composite designs. Overall, the feasibility and quality of IBM depends on two main factors: a) image quality and resolution; and b) image recognition, which involves extracting modelling information from the image, such as image segmentation and image structure tensor computation. As regards image quality and resolution, a detailed discussion can be found in section: *Capturing image data*. It is noteworthy that small-angle X-ray scattering (SAXS) tensor tomography (see sub-section: *Small-angle scattering tensor tomography*) can provide precise tensile modulus predictions for voxel sizes up to fifteen times larger than the fibre diameter.[30]

Since, image recognition is strongly correlated with the type of composite material studied, this section considers different types of composite materials in turn. For unidirectional composite laminates, the most straightforward image recognition approach is to identify individual fibres from the image, making the study of fibre misalignments/waviness highly intuitive and compelling, including fibre centre line identification[217,218] and machine learning (ML).[219] Structure tensor methods (see section: *Constitutive equations*)[121] are a good choice to process the images when their resolution is limited. There are two methods used in conjunction with the structure tensor method to enable IBM stiffness prediction. The first are **segmentation-based methods**, such as thresholding and clustering. For example, Straumit et al.[44] combined the structure tensor and K-means segmentation method to estimate the modulus of misaligned flax fibres in quasi-unidirectional composites. The second are **non-segmentation-based methods**, meaning directly packaging multiple pixels into finite element model elements. In most cases, these elements are a kind of 'composite material', and the structure tensor provides the local coordinate system and orientation in order to calculate their material properties. For example, Sabuncuoglu et al.[128] employed a voxel approach (within VoxTex and without segmentation) to evaluate fibre orientation and local stiffness variations caused by embedded microvascular channels in a non-crimp fabric composite.

With regard to woven and braided composites, IBM studies are not as extensive as those on unidirectional composite laminates. Such studies have been hampered by the lack of suitable data segmentation methods. In this respect woven composites are easier to segment than braided composites because the yarn angle differences in woven composites are more pronounced (usually 0/90°), making the yarns (including warp and weft) easier to identify, enabling structure tensor and ML methods. For example, Liu et al.[89] employed voxel models (using structure tensors) derived from X-CT images to predict elastic properties. For braided composites,[220] segmentation can be difficult to accomplish as they exhibit strong periodicity in both the circumferential and axial directions and typically have small braiding angles. Consequently, reports to date have required lots of manual intervention. For example, Liu et al.[221] refined mesoscale models for five-directional braided composites, incorporating fabric compaction and yarn torsion to enhance the geometric model. However, recent progress on automated segmentation of 2D braided CFRP tubes using fibre-tracking methods (see section 3.1.5) is compared against an idealised textile model, which is formed by sweeping an ellipse, constrained to a fixed interface, along the mathematical path defined by the braiding process, in Figure 14. It is evident that the idealised model gives rise to a gap where the bundles cross, which decreases the stress distribution on the interface of cross-section area, compared to the IBM. While the predicted elastic properties are similar (Figure 14(c)) it is likely that this would lead to differences in the initiation of damage.

Thermal and transport properties

Given the importance of ceramic matrix composites (CMCs) and carbon-carbon (C/C) composites for high-temperature applications it is not surprising that much of the literature on IBM of these materials focuses on determining thermal properties, e.g., the linear thermo-elastic response[135,222] or the thermal conductivity.[223–226] For example, researchers[223,224] have determined the thermal conductivity of respectively 2D C/C and 2.5D CMC from image-based models which include material porosity. Lopez et al.[226] suggested a methodology using the advanced reduced-order modelling and machine learning to efficiently compute thermal properties on the images for a range of values of porosities and fibre distributions. Zahid et al.[225] accounted for an imperfect interface and contact conductance when IBM a 4D C/C, which led to more favourable results than idealised modelling[227]Foster et al.[136] used U-Net, a deep convolutional neural network implemented in Dragonfly, to separate the warp and weft tows of a compression-moulded silica phenolic composite comprising an 8-harness satin (8HS) silica fibre cloth. The local tow orientation vector, describing the longitudinal direction of the filaments in the fabric, was determined using the structure tensor analysis of the images. The in-plane conductivities were well matched, but the out of plane (OOP) conductivity derived from the image-based geometries showed a much more significant deviation from the analytical model when compared to the in-plane values.

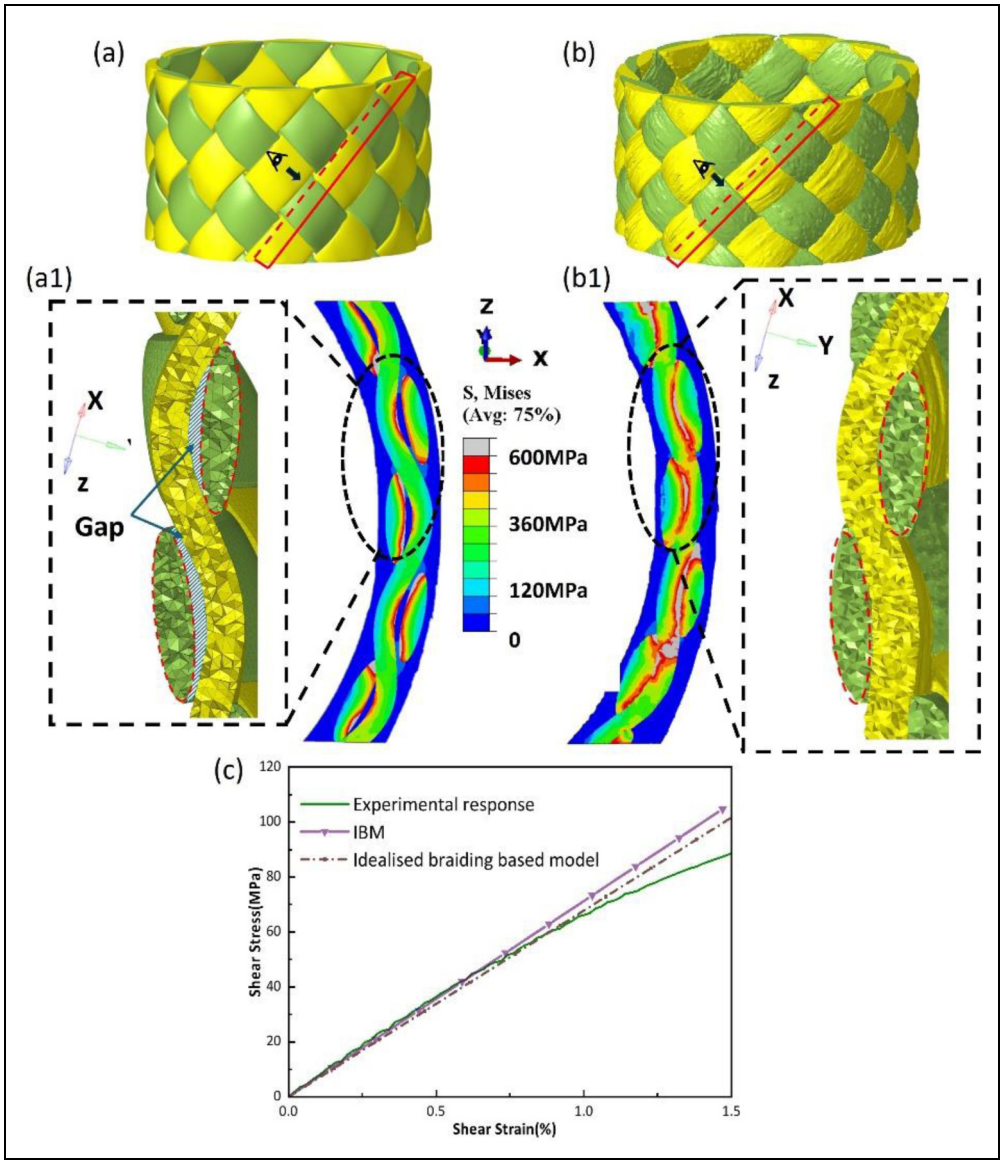

Figure 14. The comparison of the predictions of the elastic behaviour of an idealised textile model (a) and an X-CT derived IBM (b) of a braided composite. (a1) and (b1) show the braided bundle geometry (left) and the corresponding elastic torsional response (right) for the two cases, (c) displays the predicted elastic strain-stress responses alongside the experimentally measured response. (Courtesy He and Withers).

This is because the analytical model could only achieve the volume fractions observed in the X-CT images at undulation values that were much lower than the observed average undulation.

The mathematical similarity between heat conduction and mass diffusion has enabled similar approaches to be applied to other transport phenomena. For instance, Sinchuk et al.[228,229] and Cao et al.[230] employed image-based models to assess moisture diffusion in PMC and to predict the resulting hygroscopic stresses, emphasizing the significant influence of porosity on these processes. Image-based models have also proven valuable in simulating the diffusion and reaction of oxidative species in self-healing CMCs[103,231] demonstrating that the geometric variability inherent in real materials leads to non-uniform healing processes. Perrot[103] developed a 2D IBM method, enabling more accurate analysis of the self-healing processes considering oxygen diffusion, glass formation and flow dynamics, as illustrated in Figure 15. The results validated the effectiveness of the proposed method and display liquid (glassy) phase distribution, shown as Figure 15(c), which has a key influence on crack re-opening and healing process and further triggered further research on this topic, such as simulate material degradation to predict its service life.

These approaches can be readily extended to investigate other critical properties, such as thermal or electrical conductivity in fibrous systems, provided that the interfacial resistance is accurately captured.

Damage modelling

Understanding the sequence and importance of various damage mechanisms is critical for improving composite design for better efficiency and durability. Damage modelling reveals how pre-existing defects, interface strength and the composite constituents and architecture can influence the structural strength and failure processes. Damage modelling of composites spans microscale, mesoscale, and multiscale

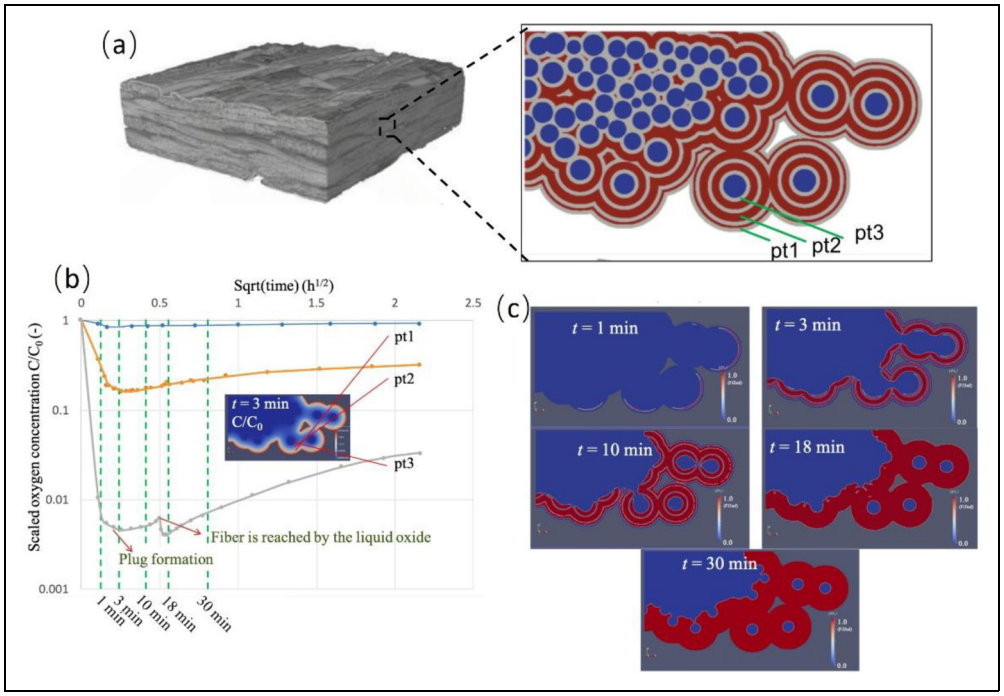

Figure 15. Modelling the oxidation of self-healing of SiC fibre ceramic-matrix composites (CMCs). (a) a mesoscale X-CT image (left), along with a magnified volume rendered image (right) showing fibres (rendered blue) and sealing matrix (red/grey). The evolution of the oxygen concentration at points pt1-3 is displayed in (b). (c) time-lapse sequence showing the predicted liquid (glassy) phase distribution from the IBM simulation.[103]

approaches, with each offering unique insights into failure mechanisms.

Regarding microscale IBM, the challenges and limitations have been discussed in sub-section: *Modelling at specific scales*. Generally, microscale IBM is a better candidate for numerically exploring the damage behaviour because it can take into account (a) defects, such as voids and fibre misalignment, and (b) the real distribution of the fibres, which can, for example, be far from ideal in natural fibre-reinforced composites. Iversen et al.[232] used fibre tracing to identify fibres of natural fibre composite and build the microscale FE model to simulate its damage behaviour, which validated that IBM is a reliable approach to include the non-uniform properties of fibres.[233,234] Liu et al.[235] used fibre centre point tracking (see sub-section: *Segmenting images into distinct phases; Fibre-tracking (tractography)*) to distinguish fibres to build a 2D IBM model of UD composites to consider the influence of fibre arrangements and resin porosity on mechanical performance. The resulting IBM accorded well with the experiment results including the compressive modulus, strength and resin porosity which strongly influence the transverse compressive performance. Wan et al.[236] employed the structure tensor method to characterise the microscale fibre distribution and geometry within sheet moulding compounds (SMC). Based on this characterisation, two distinct models were developed to analyse the material's tensile response: (a) a model incorporating the actual fibre distribution, and (b) an equivalent homogenised model. The results indicate that the IBM model (a) yields a more accurate prediction of the tensile modulus. However, both models produce comparable results in terms of tensile strength, showing no significant discrepancy.

Mesoscale modelling generally relates to textile composites (2D and 3D woven, braided etc), whose mesoscale features (tows/yarns, matrix and interface) have a key influence on the structural strength and failure mechanisms. As mentioned in sub-section: *Turning phases into finite element meshes*, the main challenge is the segmentation of the yarns/tows. Liu et al.[89] developed an IBM framework for three-dimensional woven composites utilizing the structure tensor method, aiming to explore their damage behaviour under uniaxial tensile loading. The study revealed that while the elastic response of the material remains relatively insensitive to local variations in yarn geometry, these microstructural irregularities, such as yarn unevenness and defects, play a critical role in initiating and propagating damage, thereby significantly influencing the failure mechanisms. Similarly, Mazars et al.[191] developed an IBM approach, informed by in-situ tensile experiments on CMCs, to predict the onset of damage. By incorporating the actual fibre bundle geometry, the model accurately captured the maximum strain distribution in the elastic area and effectively identified the sites of damage initiation. Machine learning has also been used by Ai et al. for yarn identification for C/SiC composites tested under tension.[237] They found that the damage initiates from porosity (see Figure 16(b)) which then grows towards the interface between yarns and matrix and finally presents as macroscale cracks. This sequence shows a high degree of consistency with in-situ tensile images (see Figure 16(c)).

Peridynamics models are well suited to simulating fracture and damage problems. Wang et al.[238] used a peridynamics model (BB-PD) based on X-CT images of a C/SiC woven CMC segmented using a deep learning-based image recognition model to predict damage under increasing tension and the results are summarised in Figure 17. As loading progresses, damage appears where a significant number of peridynamic bonds between material points begin to fracture. This develops into a crack which extends from the surface

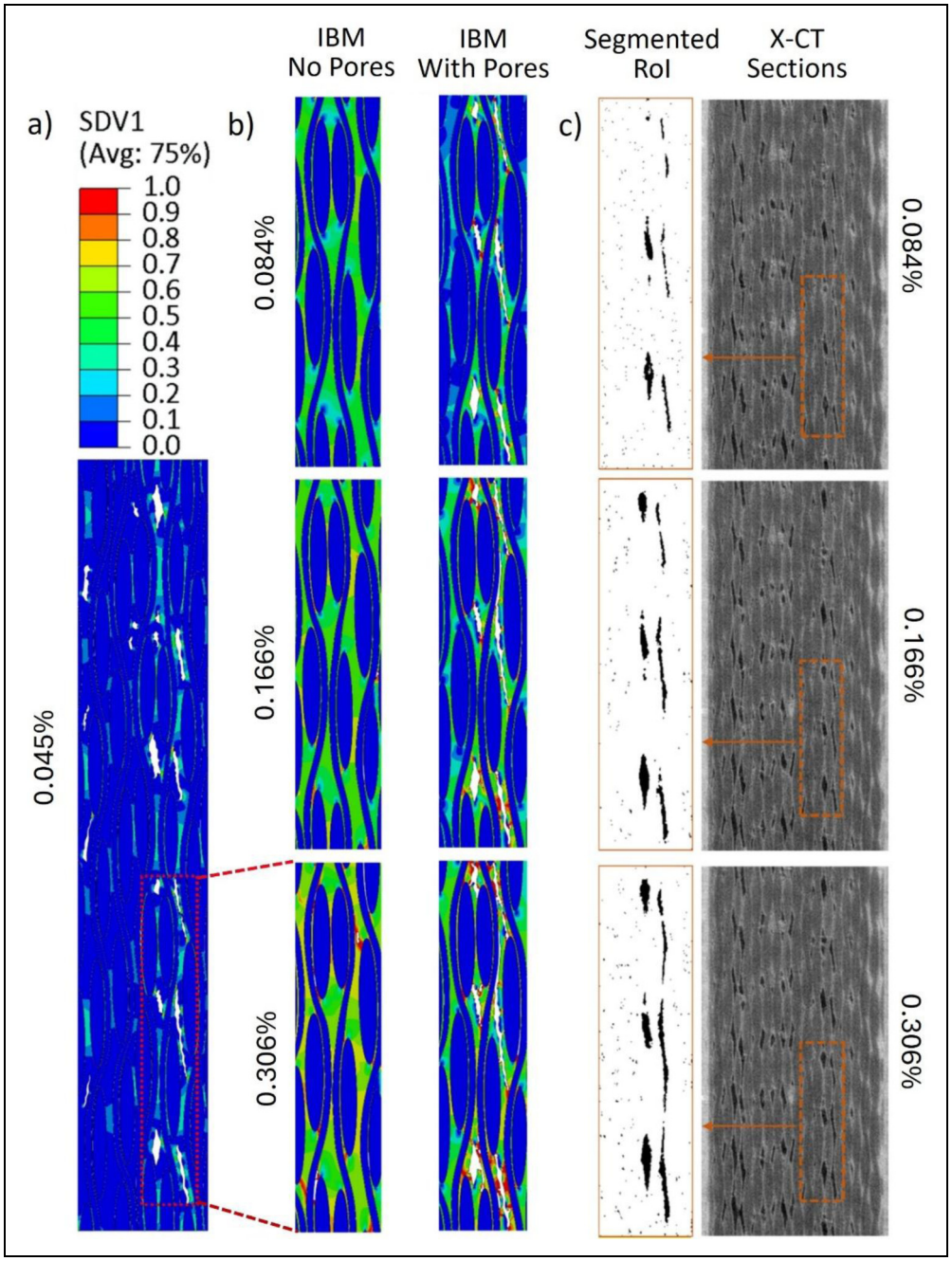

Figure 16. Evolution of damage (SDV1 = 0 to 1) for a CVI C/SiC woven composite. (a) the IBM at 0.045%, (b) regions of interest without (left) and with (right) initial porosity) and (c) in situ X-CT slices (right) and binarized damage (left) recorded at various longitudinal tensile strains after.[237]

into the interior. It is evident that damage primarily occurs at the interface between the fibres and the matrix, with minimal damage within the yarns. The image-based peridynamics model can accurately reconstruct the actual composite microstructure. It can effectively simulate various fracture phenomena such as interfacial debonding, crack propagation affected by defects, and damage to the matrix.

With regard to particulate 'composites', image-based modelling is finding extensive application for the identification of cracking processes and the associated crack paths in concrete. For example, Ren et al.[239] created a two-dimensional meso-scale image based finite element concrete model from an X-CT scan simply by greyscale thresholding comprising aggregates (here rendered blue), cement paste (grey) and voids (white) see Figure 18. Cohesive elements with traction–separation laws were used to describe the cement paste and aggregate–cement interfaces. Under tensile loading a large number of images were simulated with statistical analysis demonstrating very different load-carrying capacities and crack patterns relating to the random distribution of phases. They found that the relative strength of cement pastes and interfaces dominates the microcracking behaviour (top), which in turn affects macrocracking (middle) and hence the load-carrying capacity. The strength was also inversely proportionate to the pore volume fraction. At a local level, the results show that a large number of interfacial microcracks initiate early on and gradually become stable before the peak load (point C) is reached. It can be seen

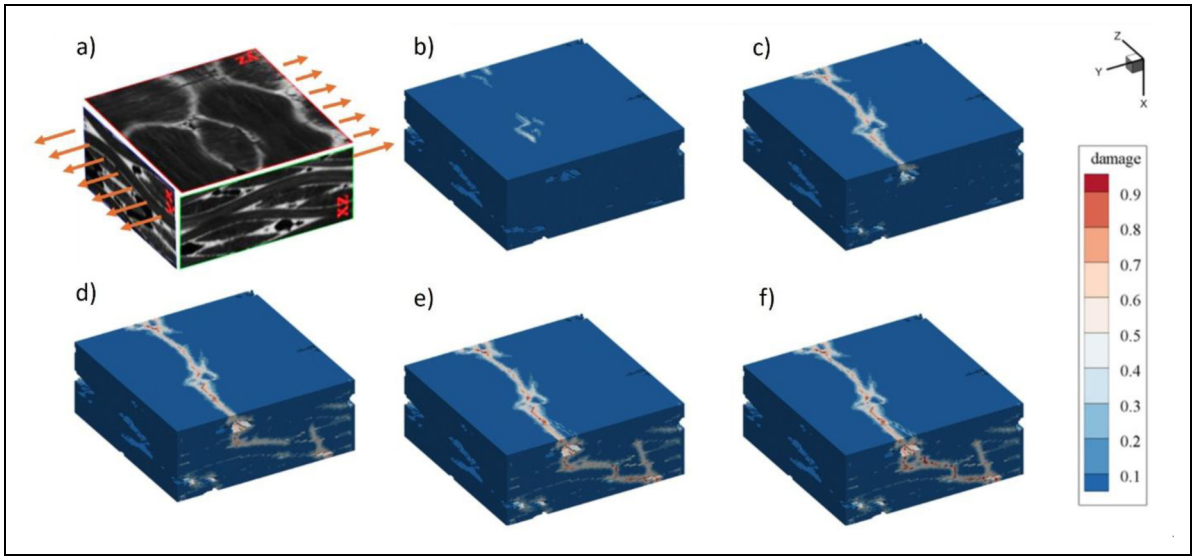

Figure 17. The 3D damage sequence for a woven C/SiC composite under a tensile load. (a) original X-CT image, (b) crack initiation, (c–e) crack growth, (f) failure stage.[238]

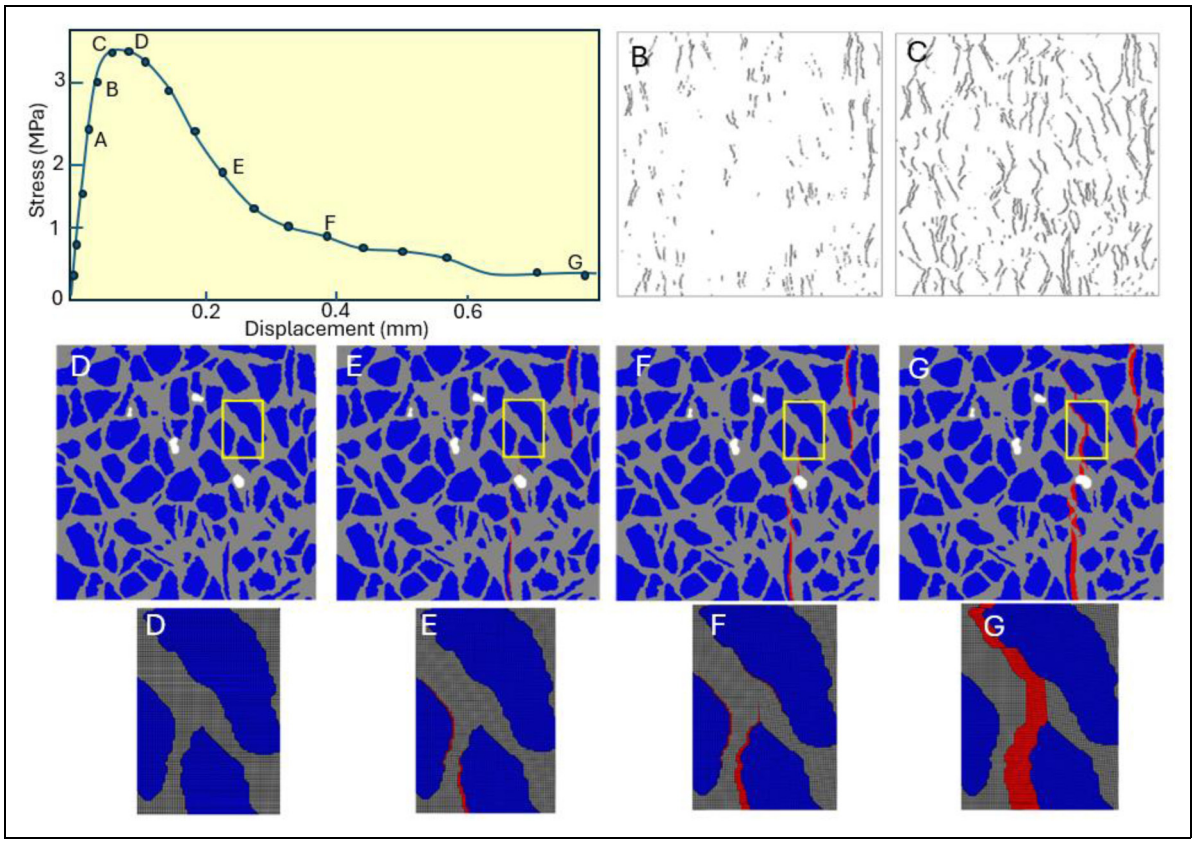

Figure 18. The evolution of pre-peak microcracking (top) and the associated macrocrack propagation (middle) and magnified region of interest (bottom) for a central cross section taken from an IBM under progressive tensile loading (horizontal axis) at the locations on the stress-displacement curve (top left) indicated by the letters. Paste is rendered grey, voids white, aggregate blue and the macrocrack red. The peak strength corresponds to stage C.[239]

that macrocracking is not evident at this point but as the displacement increases further, some aggregate–cement interfacial cracks continue to propagate and gradually coalesce with newly formed cracks to form macrocracks.

Validation with experimental results

Validation is a critical aspect of image-based modelling, ensuring that simulations reliably replicate real-world behaviour.

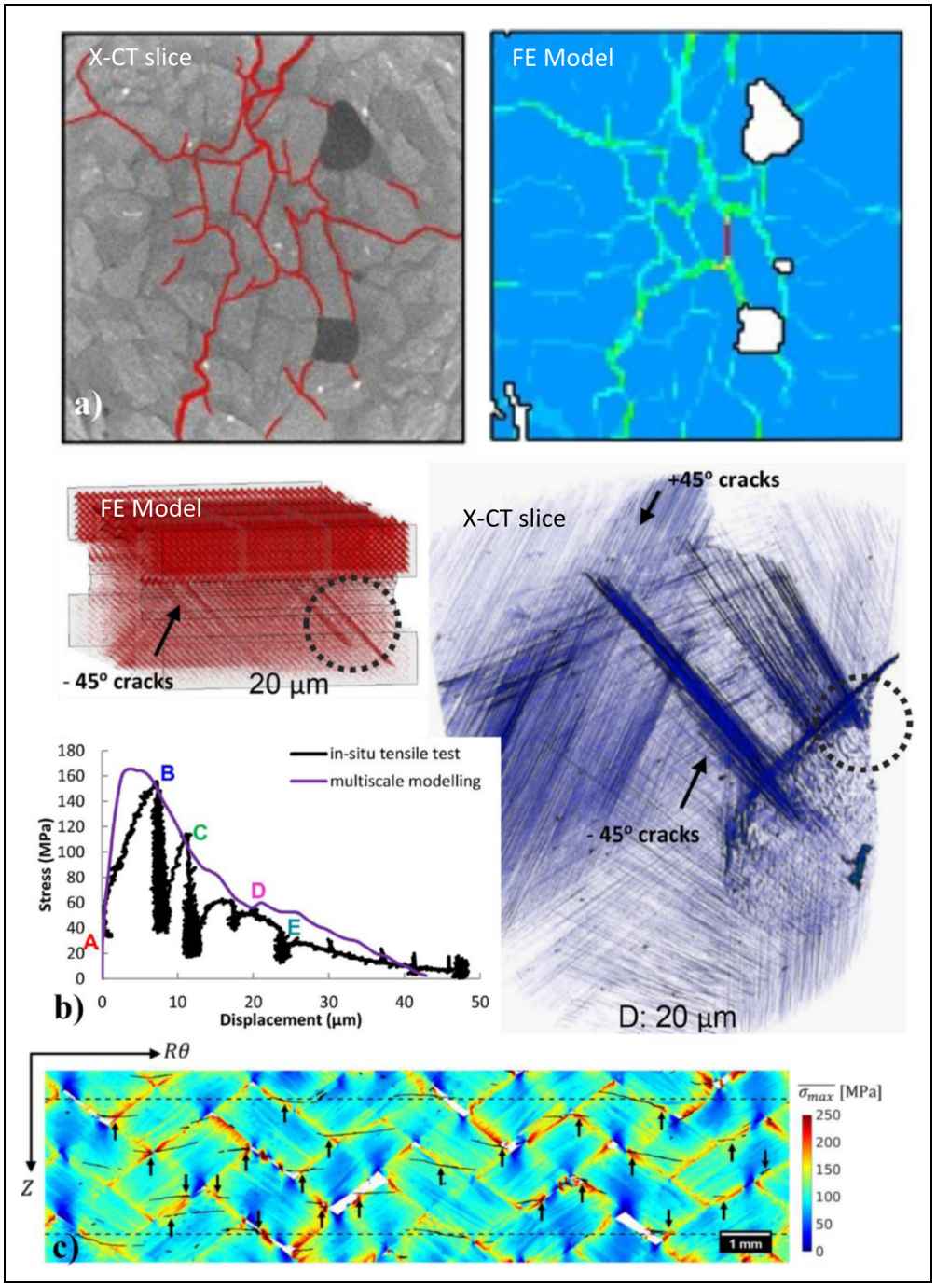

Figure 19. Comparison of image-based modelling with experiment. (a) Crack patterns on a longitudinal X-CT slice through a 40 mm concrete cube (left) under compression (vertical axis) and the predicted maximum principal strain contours for the IBM (right)[243] (b) measured and predicted stress-displacement curves for a FE multiscale IBM of a double notched cross-ply CFRP laminate tested in tension along with the predicted damage pattern (top) and the observed pattern (right),[161] (c) maximum principal stresses in the external sublayer (L4) of a braided SiC/SiC tube superimposed on the unwrapped X-CT slice with the cracks rendered black.[254]

Capturing macroscopic behaviour: A first validation step involves checking that the proposed image-based model is able to reproduce the overall macroscale behaviour of the material. Standard tensile tests on coupon samples are often used (e.g.,[44,50,221,237,240]). They provide a comparison between the experimental and simulated tensile curves (e.g., for a UD composite[232] or short fibres composites[234,241]) or directly between the experimental and simulated longitudinal Young's moduli (e.g., for a 3D printed composite[219] or a braided composite[221]). Tserpe et al.[50] proposed a more extensive experimental campaign, including compression and torsion testing to identify the transverse properties of UD CFRPs. Standard tests have also been used for validating the component properties, calculated by IBM, Straumit et al.,[44] for instance, built an IBM, considering the flax fibres misalignment of quasi-UD composites, to calculate their Young's modulus which fits well with standard tensile test.

Capturing local phenomena: Of course, the main interest in image-based models lie in their capacity to reproduce the local behaviour of the material. Imaging techniques and full-field measurement are thus invaluable tools in validating the

predictions of local behaviour. Conventional experiments can be instrumented with cameras that can be used to follow the crack propagation explicitly or, via Digital Image Correlation (DIC),[242,243] the evolution of the strain concentration field.[240]

Since many IBM models are established on the basis of X-CT, it is perhaps not surprising that time-resolved X-CT imaging (often referred to as 4D X-CT (3D + t)) is frequently used to validate the predictions of the IBM.[244–247] It can be coupled with additional post-processing techniques to validate the models, providing a better understanding of the effect of the microstructure on the behaviour of the composite, including the role of defects introduced during manufacturing and subsequent damage initiation.[242,248–250] In this respect, many X-ray CT scanners can accommodate loading or environmental stages to reveal the damage initiation and propagation sequence under increasing loads, including tension,[246] compression,[83] torsion,[247,248] bending,[245] and cyclic loading.[251,252] The direct observation of the reconstructed volume can be used to qualitatively determine the damage scenarios, highlighting the influence of the mesostructure of the material (see for example for PMCs,[248,253] CMCs,[191,249,250,254] and for concrete[242]) and as a means of verifying the veracity of the damage initiation criteria. A number of illustrative examples are shown in Figure 19 covering particulate, 2D cross-ply laminates and braided materials.

In Figure 19(a), the complex crack path formed in a concrete sample under uniaxial compression detected by X-CT agrees well with the maximum principal strain predicted by the IBM. In Figure 19(b), various competing damage mechanisms (interface sliding, debonding, matrix cracking and fibre fracture) have been explicitly included in the IBM damage model for a $(-45°/90°/+45°\ /0°\ /-45°/90°\ /+45°\ /0°)_s$ CFRP laminate giving good agreement both with the stress strain curve and the damage observed by in situ X-CT. In Figure 19(c), a large-scale image-based FFT simulation of the stresses developed during a uniaxial tensile test on a braided SiC/SiC tube, is compared with the cracking damage observed in situ by X-CT showing good agreement between the principal stresses and the location of cracks at the onset of damage. In particular, it shows how the damage arises at stress concentrations at cross-over interfaces, separated parallel interfaces and connected parallel interfaces.

For more quantitative validation, digital image correlation (DIC),[242,243,255–258] stereo-DIC[258] and digital volume correlation (DVC),[259–262] can map the 2D surface displacement, the 3D surface displacement and the 3D displacement in the bulk of the sample respectively during the experiment for direct side by side comparisons. For example, they allow the measurement of the experimental boundary conditions, which can be used in simulations.[191,250,254] Furthermore, the displacement field measured by DVC, u_{DVC}, can be expressed on an FE basis[263] and directly compared to the simulated displacement, u_{FEM}, by defining a displacement field residual ρ_{FEMU}:

$$\rho_{FEMU} = u_{FEM}(p) - u_{DVC} \tag{4}$$

where p is the vector of the model parameters. Here, the two displacement fields are expressed on the same basis. Avril et al.[264] describe five identification methods based on full-field measurement. Two methods offer the best results in terms of identified parameter uncertainties: namely, weighted finite element method updating (FEMU) and integrated digital image/volume correlation (IDIC/IDVC).[265] It has been shown that IDIC/IDVC enables the identification even when the computation of the displacement field is difficult and requires a strong regularisation.[138]

The displacement field alone is usually not sufficient to identify the constitutive parameters. For Young's moduli, for instance, a force measurement is necessary. Additional measurement modalities, such as force[266] or temperature field,[267,268] can complement the IDIC/IDVC framework.[138] Each contribution must be weighted by its uncertainty to minimise the identified parameter uncertainties. For the image contribution, this weight is the noise level. If those extra measurements are not available, additional hypotheses can be used to solve the problem. Tikhonov regularisation penalises large variations of the parameters' initial values and is relevant when confidence in these initial values is high.[269] Fixing certain parameters can also be useful. In the elastic domain, fixing one Young's modulus will allow the identification of all the other elastic moduli without the need to measure the force.[270]

Recent advancements are significantly improving the temporal resolution of validation experiments (e.g., ultra-fast imaging,[271] multi-source tomography,[272] and projection-based DVC[273,274]) which will facilitate increasing application of FEMU and IDVC for dynamic or damage accumulation studies.

Conclusions and outlook

Image-based modelling has transformed our ability to model manufacturing and the resulting behaviour of composite materials, moving the topic from the consideration of idealised systems to the study of real composite microstructures incorporating all manner of defects and features. This promises to accelerate the optimisation of manufacturing processes, focusing on those features most deleterious to performance, for example 'how deleterious are voids and fibre-free regions?' and 'is the fibre alignment good enough?' Further they enable us to design ever more complex hierarchical composite structures and reduce the cost of the current testing pyramid depicted in Figure 1.

By harnessing advanced imaging techniques and numerical methods, researchers can predict and validate properties ranging from simple elastic and transport properties to the temporal sequence of damage in 3D and its implications in terms of performance. The efficacy of toughening mechanisms and interface tailoring can be explored for realistic microstructures. The incorporation of health monitoring and self-healing agents can also be optimised.

The studies reviewed here demonstrate the transformative potential of this approach in advancing composite materials science, paving the way for innovative composite design and optimisation. As imaging and computational capabilities continue to evolve, the scope and impact of image-based modelling are expected to expand, fostering deeper integration into composite research and engineering practices. Today most of the focus has been on elastic properties. Going forwards better constitutive laws for inelastic

processes and degradation phenomena are required such that IBM can play a significant role in understanding the effect of the local microstructure on damage initiation and accumulation, both to safely predict the lifetime of real composite systems with their associated manufacturing defects, but also to help improve manufacturing processes and stimulate new composite architectures with excellent multifunctional properties.

Abbreviation summary

AFEM	augmented finite element method
AI	artificial intelligence
ANN	artificial neural network
CAD	computer aided design
CDM	continuum damage mechanics
CFRP	carbon fibre reinforced polymer
CMC	ceramic matrix composite
CNN	convolutional neural network
CZM	cohesive zone model
DIC	digital image correlation
DNN	deep neural network
DVC	digital volume correlation
GFRP	glass fibre reinforced polymer
FIB	focused ion beam
FE	finite element
FEM	finite element method
FEMU	finite element method updating
FFT	fast fourier transform
FRP	fibre reinforced polymer
FVM	finite volume method
IBM	image-based modelling
IDIC	integrated digital image correlation
IDVC	integrated digital volume correlation
IGA	isogeometric analysis
KUBCs	kinematically uniform boundary conditions
ML	machine learning
PBCs	periodic boundary conditions
PINN	physics-informed neural network
PMC	polymer matrix composite
RVE	representative volume element
SAXS	small angle X-ray scattering
SDIC	stereo digital image correlation
SEM	scanning electron microscope
SUBCs	statically uniform boundary conditions
UD	unidirectional
X-CT	X-ray computed tomography

Acknowledgements

PJW and DH would like to acknowledge the support of the Henry Royce Institute, the National X-ray Computed Tomography (NXCT) facility and an International Centre to Centre grant with the ESRF funded by EPSRC through (EP/R00661X/1, EP/S019367/1, EP/P025021/1, EP/P025498/1 EP/T02593X/1 and EP/W003333/1). PJW is grateful to Monash University for hosting his sabbatical during which time much of this review was written. MMe and CB would like to acknowledge the funding received from FWO for their postdoctoral fellowships BIOPTOUGH (12B0624N) and SUBFIRE (12A0625N). The IBSim-4i workshop (2023) is acknowledged at which the concept for this review paper originated. PJW also appreciates discussions with Dr Sam Cooper.

Funding

The authors received no financial support for the research, authorship, and/or publication of this article.

Declaration of conflicting interests

The authors declared no potential conflicts of interest with respect to the research, authorship, and/or publication of this article.

Data availability statement

The data that support the findings of this study are available from the corresponding author upon reasonable request.

ORCID iDs

Dongze He https://orcid.org/0000-0003-0983-7977
Yang Chen https://orcid.org/0000-0003-1026-0482
Christian Breite https://orcid.org/0000-0001-9695-2257
Mikhail Y Matveev https://orcid.org/0000-0002-0509-1672
Léonard Turpin https://orcid.org/0000-0001-6693-9115
Elena Syerko https://orcid.org/0009-0000-8933-5322
Guillaume Couégnat https://orcid.org/0000-0001-5711-6328
Jeroen Soete https://orcid.org/0000-0003-3357-4070
Mahoor Mehdikhani https://orcid.org/0000-0003-3989-2678
Stepan V Lomov https://orcid.org/0000-0002-8194-4913
Yentl Swolfs https://orcid.org/0000-0001-7278-3022
Philip J Withers https://orcid.org/0000-0002-1946-5647

References

1. Dunlop JW and Fratzl P. Biological composites. *Annu Rev Mater Res* 2010; 40: 1–24.
2. Seago AE, Brady P, Vigneron JP, et al. Gold bugs and beyond: a review of iridescence and structural colour mechanisms in beetles (Coleoptera). *J R Soc Interface* 2009; 6: S165–S184.
3. Ma Y, Aichmayer B, Paris O, et al. The grinding tip of the sea urchin tooth exhibits exquisite control over calcite crystal orientation and mg distribution. *Proc Natl Acad Sci U S A* 2009; 106: 6048–6053.
4. Arteiro A, Catalanotti G, Reinoso J, et al. Simulation of the mechanical response of thin-ply composites: from computational micro-mechanics to structural analysis. *Arch Comput Methods Eng* 2019; 26: 1445–1487.
5. Ghosh S, Dimiduk D and Furrer D. Statistically equivalent representative volume elements (SERVE) for material behaviour analysis and multiscale modelling. *Int Mater Rev* 2023; 68: 1158–1191.
6. Shahzamanian MM, Akhtar SS, Arif AFM, et al. Thermo-mechanical properties prediction of Ni-reinforced Al2O3 composites using micro-mechanics based representative volume elements. *Sci Rep* 2022; 12: 11076.
7. Bargmann S, Klusemann B, Markmann J, et al. Generation of 3D representative volume elements for heterogeneous materials: a review. *Prog Mater Sci* 2018; 96: 322–384.
8. Garcea S, Wang Y and Withers PJ. X-ray computed tomography of polymer composites. *Compos Sci Technol* 2018; 156: 305–319.
9. Guild FJ and Summerscales J. Microstructural image analysis applied to fibre composite materials: a review. *Compos* 1993; 24: 383–393.

10. Jensen DJ, Lilholt H and Withers PJ. Determination of fibre orientations in composites with short fibres. In: *Proceedings of the Riso International Symposium on Metallurgy and Materials Science*, 1988, pp. 413–420.
11. From PS and Pyrz R. Computer assisted stereology of short fibre composites, I: determination of fibre length distribution. *Sci Eng Compos Mater* 1999; 8: 143–158.
12. Lukas D and Chaloupek J. Understanding the three-dimensional structure of fibrous materials using stereology. In: Pan N and Gibson P (eds) *Thermal and moisture transport in fibrous materials*. Cambridge: Woodhead publishing, 2006, pp.42–101.
13. Kench S and Cooper SJ. Generating three-dimensional structures from a two-dimensional slice with generative adversarial network-based dimensionality expansion. *Nat Mach Intell* 2021; 3: 299–305.
14. Groeber MA and Jackson MA. DREAM. 3D: a digital representation environment for the analysis of microstructure in 3D. *Integr Mater Manuf Innov* 2014; 3: 56–72.
15. Bentz DP and Bentz DP. *CEMHYD3D: A three-dimensional cement hydration and microstructure development modelling package. Version 2.0*. US Department of Commerce, National Institute of Standards and Technology, 2000.
16. Winiarski B, Gholinia A, Mingard K, et al. Broad ion beam serial section tomography. *Ultramicroscopy* 2017; 172: 52–64.
17. Echlin MP, Burnett TL, Polonsky AT, et al. Serial sectioning in the SEM for three dimensional materials science. *Curr Opin Solid State Mater Sci* 2020; 24: 100817.
18. Zankel A, Wagner J and Poelt P. Serial sectioning methods for 3D investigations in materials science. *Micron* 2014; 62: 66–78.
19. Jung JM, Yoo JH, Jeong HJ, et al. Three-dimensional characterization of SiC particle-reinforced al composites using serial sectioning tomography and thermo-mechanical finite element simulation. *Metall Mater Trans A* 2014; 45: 5679–5690.
20. Hakim I, Schumacher D, Sundar V, et al. Volume imaging NDE and serial sectioning of carbon fiber composites. In: *AIP Conf Proc*, 2018. AIP Publishing.
21. Withers PJ, Bouman C, Carmignato S, et al. X-ray computed tomography. *Nat Rev Methods Primers* 2021; 1: 18.
22. Maire E and Withers PJ. Quantitative X-ray tomography. *Int Mater Rev* 2013; 59: 1–43.
23. Wang Y, Garcea SC and Withers PJ. 7.6 Computed tomography of composites. In: Beaumont PWR and Zweben CH (eds) *Comprehensive composite materials II*. Oxford: Elsevier, 2018, pp.101–118.
24. Landis EN and Keane DT. X-ray microtomography. *Mater Charact* 2010; 61: 1305–1316.
25. Yu B, Bradley RS, Soutis C, et al. A comparison of different approaches for imaging cracks in composites by X-ray microtomography. *Philos Trans A Math Phys Eng Sci* 2016; 374: 20160037.
26. Snigirev A, Snigireva I, Kohn V, et al. On the possibilities of x-ray phase contrast microimaging by coherent high-energy synchrotron radiation. *Rev Sci Instrum* 1995; 66: 5486–5492.
27. Wilkins S, Gureyev TE, Gao D, et al. Phase-contrast imaging using polychromatic hard X-rays. *Nature* 1996; 384: 335–338.
28. Paganin D, Mayo SC, Gureyev TE, et al. Simultaneous phase and amplitude extraction from a single defocused image of a homogeneous object. *J Microsc* 2002; 206: 33–40.
29. Fransson M, Cordonnier B, Zimmermanns R, et al. A comparison of stitching techniques to reconstruct large volume x-ray tomography of batteries. *Tomogr Mater Struct* 2024; 5: 100029.
30. Auenhammer RM, Kim J, Oddy C, et al. X-ray scattering tensor tomography based finite element modelling of heterogeneous materials. *npj Comput Mater* 2024; 10: 50.
31. Liebi M, Georgiadis M, Menzel A, et al. Nanostructure surveys of macroscopic specimens by small-angle scattering tensor tomography. *Nature* 2015; 527: 349–352.
32. Kagias M, Wang Z, Birkbak ME, et al. Diffractive small angle X-ray scattering imaging for anisotropic structures. *Nat Commun* 2019; 10: 5130.
33. Kim J, Kagias M, Marone F, et al. X-ray scattering tensor tomography with circular gratings. *Appl Phys Lett* 2020; 116: 134102.
34. Kim J, Slyamov A, Lauridsen E, et al. Macroscopic mapping of microscale fibers in freeform injection molded fiber-reinforced composites using X-ray scattering tensor tomography. *Compos B* 2022; 233: 109634.
35. Kagias M, Wang Z, Villanueva-Perez P, et al. 2D-Omnidirectional Hard-X-Ray scattering sensitivity in a single shot. *Phys Rev Lett* 2016; 116: 093902.
36. Swaminathan S, Ghosh S and Pagano N. Statistically equivalent representative volume elements for unidirectional composite microstructures: part I-without damage. *J Compos Mater* 2006; 40: 583–604.
37. Kanit T, Forest S, Galliet I, et al. Determination of the size of the representative volume element for random composites: statistical and numerical approach. *IJSS* 2003; 40: 3647–3679.
38. Drugan WJ and Willis JR. A micromechanics-based nonlocal constitutive equation and estimates of representative volume element size for elastic composites. *J Mech Phys Solids* 1996; 44: 497–524.
39. Sezgin M and Sankur B. Survey over image thresholding techniques and quantitative performance evaluation. *J Electron Imaging* 2004; 13: 146–168.
40. Rayed ME, Islam SS, Niha SI, et al. Deep learning for medical image segmentation: state-of-the-art advancements and challenges. *Inform Med Unlocked* 2024; 47: 101504.
41. Jasim W and Mohammed RJ. A survey on segmentation techniques for image processing. *Iraqi J Electr Electron Eng* 2021; 17: 73–93.
42. Sosa-Rey F, Abderrafai Y, Lewis AD, et al. Openfiberseg: open-source segmentation of individual fibers and porosity in tomographic scans of additively manufactured short fiber reinforced composites. *Compos Sci Technol* 2022; 226: 109497.
43. Zaitoun NM and Aqel MJ. Survey on image segmentation techniques. *Procedia Comput Sci* 2015; 65: 797–806.
44. Straumit I, Vandepitte D, Wevers M, et al. Identification of the flax fibre modulus based on an impregnated quasi-unidirectional fibre bundle test and X-ray computed tomography. *Compos Sci Technol* 2017; 151: 124–130.
45. Yousaf Z, Withers PJ and Potluri P. Compaction, nesting and image based permeability analysis of multi-layer dry preforms by computed tomography (CT). *Compos Struct* 2021; 263: 113676.
46. Yousaf Z, Potluri P, Withers PJ, et al. Digital element simulation of aligned tows during compaction validated by computed tomography (CT). *IJSS* 2018; 154: 78–87.
47. Jeppesen N, Mikkelsen L, Dahl A, et al. Quantifying effects of manufacturing methods on fiber orientation in

unidirectional composites using structure tensor analysis. *Compos A* 2021; 149: 106541.
48. Sinchuk Y, Kibleur P, Aelterman J, et al. Variational and deep learning segmentation of very-low-contrast X-ray computed tomography images of carbon/epoxy woven composites. *Materials (Basel)* 2020; 13: 936.
49. Du Y, Zhang D, Wang L, et al. Damage mechanism characterisation of plain weave ceramic matrix composites under in-plane shear using in-situ X-ray micro-CT and deep-learning-based image segmentation. *J Eur Ceram Soc* 2024; 44: 142–153.
50. Tserpes K, Stamopoulos A and Pantelakis SG. A numerical methodology for simulating the mechanical behavior of CFRP laminates containing pores using X-ray computed tomography data. *Compos B* 2016; 102: 122–133.
51. Tretiak I and Smith RA. A parametric study of segmentation thresholds for X-ray CT porosity characterisation in composite materials. *Compos A* 2019; 123: 10–24.
52. Aziz AR, Ali M, Zeng X, et al. Transverse permeability of dry fiber preforms manufactured by automated fiber placement. *Compos Sci Technol* 2017; 152: 57–67.
53. Pidou-Brion V and Le Guilloux Y. Active yarn meshes for segmentation on X-ray computed tomography of textile composite materials at the mesoscopic scale. *Compos Struct* 2022; 281: 115084.
54. Galvez-Hernandez P and Kratz J. The effect of convolutional neural network architectures on phase segmentation of composite material X-ray micrographs. *J Compos Mater* 2023; 57: 2899–2918.
55. Upadhyay S, Smith AG, Vandepitte D, et al. Deep-learning versus greyscale segmentation of voids in X-ray computed tomography images of filament-wound composites. *Compos A* 2024; 177: 107937.
56. Ali MA, Umer R, Khan KA, et al. XCT-scan assisted flow path analysis and permeability prediction of a 3D woven fabric. *Compos B* 2019; 176: 107320.
57. Patel DK, Waas AM and Yen C-F. Direct numerical simulation of 3D woven textile composites subjected to tensile loading: an experimentally validated multiscale approach. *Compos B* 2018; 152: 102–115.
58. Smith AG, Han E, Petersen J, et al. Rootpainter: deep learning segmentation of biological images with corrective annotation. *New Phytol* 2022; 236: 774–791.
59. Upadhyay S, George Smith A, Vandepitte D, et al. Deep-learning versus greyscale segmentation of voids in X-ray computed tomography images of filament-wound composites. *Compos A* 2024; 177: 107937.
60. Emerson MJ, Jespersen KM, Dahl AB, et al. Individual fibre segmentation from 3D X-ray computed tomography for characterising the fibre orientation in unidirectional composite materials. *Compos A* 2017; 97: 83–92.
61. Huang W, Causse P, Brailovski V, et al. Reconstruction of mesostructural material twin models of engineering textiles based on micro-CT aided geometric modeling. *Compos A* 2019; 124: 105481.
62. Tian W, Qi L, Chao X, et al. Periodic boundary condition and its numerical implementation algorithm for the evaluation of effective mechanical properties of the composites with complicated micro-structures. *Compos B* 2019; 162: 1–10.
63. Yang B, Feng Y, Béguin C, et al. Open source tool for micro-CT aided meso-scale modeling and meshing of complex textile composite structures. *Compos Sci Technol* 2025; 259: 110940.
64. Little JE, Yuan X and Jones MI. Characterisation of voids in fibre reinforced composite materials. *NDT E Int* 2012; 46: 122–127.
65. Zeng X, Brown LP, Endruweit A, et al. Geometrical modelling of 3D woven reinforcements for polymer composites: prediction of fabric permeability and composite mechanical properties. *Compos A* 2014; 56: 150–160.
66. Nikishkov G, Nikishkov Y and Makeev A. Finite element mesh generation for composites with ply waviness based on X-ray computed tomography. *Adv Eng Softw* 2013; 58: 35–44.
67. Wintiba B, Vasiukov D, Panier S, et al. Automated reconstruction and conformal discretization of 3D woven composite CT scans with local fiber volume fraction control. *Compos Struct* 2020; 248: 112438.
68. Gommer F, Endruweit A and Long AC. Analysis of filament arrangements and generation of statistically equivalent composite micro-structures. *Compos Sci Technol* 2014; 99: 45–51.
69. Naouar N, Vidal-Salle E, Schneider J, et al. 3D Composite reinforcement meso FE analyses based on X-ray computed tomography. *Compos Struct* 2015; 132: 1094–1104.
70. Auenhammer RM, Jeppesen N, Mikkelsen LP, et al. Robust numerical analysis of fibrous composites from X-ray computed tomography image data enabling low resolutions. *Compos Sci Technol* 2022; 224: 109458.
71. Jeppesen N, Christensen AN, Dahl VA, et al. Sparse layered graphs for multi-object segmentation. In: *Proceedings of the IEEE/CVF Conference on Computer Vision and Pattern Recognition*, 2020, pp. 12777–12785.
72. Bénézech J and Couégnat G. Variational segmentation of textile composite preforms from X-ray computed tomography. *Compos Struct* 2019; 230: 111496.
73. Yang B, Béguin C, Causse P, et al. Tomographic modeling and internal structure analysis of engineering textiles: a parametric approach. *Compos Struct* 2025; 352: 118679.
74. Madra A, Breitkopf P, Rassineux A, et al. Image-based model reconstruction and meshing of woven reinforcements in composites. *IJNME* 2017; 112: 1235–1252.
75. Yang H, Wang W, Shang J, et al. Segmentation of computed tomography images and high-precision reconstruction of rubber composite structure based on deep learning. *Compos Sci Technol* 2021; 213: 108875.
76. Aljuaid A and Anwar M. Survey of supervised learning for medical image processing. *SN Comput Sci* 2022; 3: 292.
77. Raza K and Singh NK. A tour of unsupervised deep learning for medical image analysis. *Curr Med Imaging* 2021; 17: 1059–1077.
78. Yao W, Bai J, Liao W, et al. From CNN to transformer: a review of medical image segmentation models. *J Imaging Inform Med* 2024; 37: 1529–1547.
79. Badran A, Marshall D, Legault Z, et al. Automated segmentation of computed tomography images of fiber-reinforced composites by deep learning. *J Mater Sci* 2020; 55: 16273–16289.
80. Blusseau S, Wielhorski Y, Haddad Z, et al. Instance segmentation of 3D woven fabric from tomography images by deep learning and morphological pseudo-labeling. *Compos B* 2022; 247: 110333.
81. Ali MA, Guan Q, Umer R, et al. Deep learning based semantic segmentation of μCT images for creating digital material twins of fibrous reinforcements. *Compos A* 2020; 139: 106131.

82. Mendoza A, Trullo R and Wielhorski Y. Descriptive modeling of textiles using FE simulations and deep learning. *Compos Sci Technol* 2021; 213: 108897.
83. Wang Y, Emerson MJ, Conradsen K, et al. Evolution of fibre deflection leading to kink-band formation in unidirectional glass fibre/epoxy composite under axial compression. *Compos Sci Technol* 2021; 213: 108929.
84. Czabaj MW, Riccio ML and Whitacre WW. Numerical reconstruction of graphite/epoxy composite microstructure based on sub-micron resolution X-ray computed tomography. *Compos Sci Technol* 2014; 105: 174–182.
85. Prajapati A. *Multiscale quantification of damage in composite structures*. United Kingdom: The University of Manchester, 2023.
86. Gommer F, Wedgwood KC and Brown LP. Stochastic reconstruction of filament paths in fibre bundles based on two-dimensional input data. *Compos A* 2015; 76: 262–271.
87. Amjad K, Christian W, Dvurecenska K, et al. Computationally efficient method of tracking fibres in composite materials using digital image correlation. *Compos A* 2020; 129: 105683.
88. Mehdikhani M, Breite C, Swolfs Y, et al. Combining digital image correlation with X-ray computed tomography for characterization of fiber orientation in unidirectional composites. *Compos A* 2021; 142: 106234.
89. Liu Y, Straumit I, Vasiukov D, et al. Prediction of linear and non-linear behavior of 3D woven composite using mesoscopic voxel models reconstructed from X-ray microtomography. *Compos Struct* 2017; 179: 568–579.
90. Zheng T, Guo L, Tang Z, et al. Comparison of progressive damage simulation of 3D woven composites between voxel and conformal discretization models. *Mech Mater* 2021; 158: 103860.
91. Ali MA, Umer R, Khan KA, et al. In-plane virtual permeability characterization of 3D woven fabrics using a hybrid experimental and numerical approach. *Compos Sci Technol* 2019; 173: 99–109.
92. Ali MA, Umer R, Khan KA, et al. Non-destructive evaluation of through-thickness permeability in 3D woven fabrics for composite fan blade applications. *Aerosp Sci Technol* 2018; 82: 520–533.
93. Doitrand A, Fagiano C, Irisarri F-X, et al. Comparison between voxel and consistent meso-scale models of woven composites. *Compos A* 2015; 73: 143–154.
94. Rassineux A. Robust conformal adaptive meshing of complex textile composites unit cells. *Compos Struct* 2022; 279: 114740.
95. Matveev MY, Brown LP and Long AC. Efficient meshing technique for textile composites unit cells of arbitrary complexity. *Compos Struct* 2020; 254: 112757.
96. Fourrier G, Rassineux A, Leroy F-H, et al. Automated conformal mesh generation chain for woven composites based on CT-scan images with low contrasts. *Compos Struct* 2023; 308: 116673.
97. Sinchuk Y, Shishkina O, Gueguen M, et al. X-ray CT based multi-layer unit cell modeling of carbon fiber-reinforced textile composites: segmentation, meshing and elastic property homogenization. *Compos Struct* 2022; 298: 116003.
98. Naouar N, Vasiukov D, Park C, et al. Meso-FE modelling of textile composites and X-ray tomography. *J Mater Sci* 2020; 55: 16969–16989.
99. Seon G, Nikishkov Y, Makeev A, et al. Mesh morphing methodology for strength predictions in composites. *Compos Struct* 2016; 140: 612–620.
100. Mazumder A, Wang Y and Yen C-F. A structured method to generate conformal FE mesh for realistic textile composite micro-geometry. *Compos Struct* 2020; 239: 112032.
101. Higuchi R, Yokozeki T, Nishida K, et al. High-fidelity computational micromechanics of composite materials using image-based periodic representative volume element. *Compos Struct* 2024; 328: 117726.
102. Wijaya W, Kelly P and Bickerton S. A novel methodology to construct periodic multi-layer 2D woven unit cells with random nesting configurations directly from μCT-scans. *Compos Sci Technol* 2020; 193: 108125.
103. Perrot G, Couégnat G, Ricchiuto M, et al. Image-Based numerical modeling of self-healing in a ceramic-matrix minicomposite. *Ceramics* 2019; 2: 308–326.
104. Creveling PJ, Fisher J, Dahlkamp C, et al. Modeling as-manufactured fiber-reinforced microstructures based on X-ray microcomputed tomography. *Compos Sci Technol* 2021; 214: 109004.
105. Creveling PJ, Whitacre WW and Czabaj MW. A fiber-segmentation algorithm for composites imaged using X-ray microtomography: development and validation. *Compos A* 2019; 126: 105606.
106. Whitacre W and Czabaj M. Automated 3D digital reconstruction of fiber reinforced polymer composites. In: *AIAA Guidance, Navigation, and Control Conference*, 2015, pp.0342.
107. Whitacre W and Czabaj M. Extension of automated 3D digital reconstruction to multi-directional fiber reinforced composite microstructures. In: *57th AIAA/ASCE/AHS/ASC Structures, Structural Dynamics, and Materials Conference*, 2016, pp.1233.
108. Dahl VA, Emerson MJ, Trinderup CH, et al. Content-based propagation of user markings for interactive segmentation of patterned images. In: *Proceedings of the IEEE/CVF Conference on Computer Vision and Pattern Recognition Workshops*, 2020, pp.994–995.
109. Emerson MJ, Dahl AB, Conradsen K, et al. Insegt fibre: a user-friendly software for individual fibre segmentation. In: *22nd International Conference on Composite Materials 2019* (ed Adrian M, Chun W and Bronwyn F), Melbourne, Australia, 11-16, August 2019.
110. Breite C. Aligning fibre break models for composites with the observable micro-scale material behaviour. PhD Thesis, Leuven: KU Leuven, 2021.
111. Breite C, Melnikov A, Turon A, et al. Detailed experimental validation and benchmarking of six models for longitudinal tensile failure of unidirectional composites. *Compos Struct* 2022; 279: 114828.
112. Emerson MJ, Wang Y, Withers PJ, et al. Quantifying fibre reorientation during axial compression of a composite through time-lapse X-ray imaging and individual fibre tracking. *Compos Sci Technol* 2018; 168: 47–54.
113. Lee S, Hong C and Ji W. In situ micromechanical analysis of discontinuous fiber-reinforced composite material based on DVC strain and fiber orientation fields. *Compos B* 2022; 247: 110361.
114. Huang CT, Chen XW and Fu WW. Investigation on the fiber orientation distributions and their influence on the mechanical

property of the co-injection molding products. *Polymers (Basel)* 2019; 12: 24.
115. Han S, Li Q, Newton MAA, et al. Research on cotton yarn based on synchrotron radiation 3D micro-CT imaging. *Fibers and Polymers* 2024; 25: 543–555.
116. Melenka GW and Gholami A. Fiber identification of braided composites using micro-computed tomography. *Compos Commun* 2021; 27: 100813.
117. Verho T, Fortino S, Hradil P, et al. Biocomposite modeling by tomographic feature extraction and synthetic microstructure reconstruction. *Compos Sci Technol* 2022; 230: 109713.
118. Srisuriyachot J, Bénézech J, Couégnat G, et al. Synchrotron micro-CT in kink-band formation of UD-CFRP laminates with microdefects. *Compos B* 2023; 266: 111038.
119. Salling FB, Jeppesen N, Sonne MR, et al. Individual fibre inclination segmentation from X-ray computed tomography using principal component analysis. *J Compos Mater* 2022; 56: 83–98.
120. Baran I, Straumit I, Shishkina O, et al. X-ray computed tomography characterization of manufacturing induced defects in a glass/polyester pultruded profile. *Compos Struct* 2018; 195: 74–82.
121. Straumit I, Lomov SV and Wevers M. Quantification of the internal structure and automatic generation of voxel models of textile composites from X-ray computed tomography data. *Compos A* 2015; 69: 150–158.
122. Mersmann C. Industrializing metrology—machine vision integration in composites production. *CIRP Ann* 2011; 60: 511–514.
123. Nguyen NQ, Mehdikhani M, Straumit I, et al. Micro-CT measurement of fibre misalignment: application to carbon/epoxy laminates manufactured in autoclave and by vacuum assisted resin transfer moulding. *Compos A* 2018; 104: 14–23.
124. Nelson L, Smith R and Mienczakowski M. Ply-orientation measurements in composites using structure-tensor analysis of volumetric ultrasonic data. *Compos A* 2018; 104: 108–119.
125. Sapozhnikov SB, Swolfs Y and Lomov SV. Mode I and II interlaminar critical energy release rates in all-carbon interlayer unidirectional fibre-hybrids based on ultrahigh-modulus and high-strength fibres. *Compos Struct* 2020; 236: 111886.
126. Sapozhnikov S, Swolfs Y and Lomov S. Pseudo-ductile unidirectional high modulus/high strength carbon fibre hybrids using conventional ply thickness prepregs. *Compos B* 2020; 198: 108213.
127. Lomov SV and Abaimov SG. Influence of the nanostitch sensor embedment on the fibrous microstructure of glass fiber prepreg laminates. *Polymers (Basel)* 2022; 14: 4644.
128. Sabuncuoglu B, Tanabi H, Soete J, et al. Micro-CT analysis of deviations in fiber orientation and composite stiffness near the microvascular channels embedded in glass-fiber reinforced composites. *Compos Struct* 2020; 237: 111896.
129. Straumit I, Hahn C, Winterstein E, et al. Computation of permeability of a non-crimp carbon textile reinforcement based on X-ray computed tomography images. *Compos A* 2016; 81: 289–295.
130. Jeppesen N, Dahl V, Christensen A, et al. Characterization of the fiber orientations in non-crimp glass fiber reinforced composites using structure tensor. In: *IOP Conference Series: Materials Science and Engineering*, 2020, p. 012037. IOP Publishing.
131. Auenhammer RM, Jeppesen N, Mikkelsen LP, et al. X-ray computed tomography data structure tensor orientation mapping for finite element models—STXAE. *Software Impacts* 2022; 11: 100216.
132. Barburski M, Straumit I, Zhang X, et al. Micro-CT analysis of internal structure of sheared textile composite reinforcement. *Compos A* 2015; 73: 45–54.
133. Zhu J, Ma Y, Ding G, et al. Extraction of the microstructure of wool fabrics based on structure tensor. *Sensors (Basel)* 2023; 23: 6813.
134. Aravand MA, Shishkina O, Straumit I, et al. Internal geometry of woven composite laminates with "fuzzy" carbon nanotube grafted fibers. *Compos A* 2016; 88: 295–304.
135. Yu G, Jia Y, Dong C, et al. Geometric parameters characterization of minicomposite and modulus prediction of 2D composite based on X-ray computed tomography. *Ceram Int* 2021; 47: 30391–30398.
136. Foster CW, Collins LN, Panerai F, et al. Assessing thermophysical properties of parameterized woven composite models using image-based simulations. *Compos Sci Technol* 2023; 241: 110136.
137. Pannier Y, Coupé P, Garrigues T, et al. Automatic segmentation and fibre orientation estimation from low resolution X-ray computed tomography images of 3D woven composites. *Compos Struct* 2023; 318: 117087.
138. Turpin L, Roux S, Bénézech J, et al. Quantitative thermomechanical characterisation of 3D-woven SiC/SiC composites from in-situ tomographic and thermographic imaging. *Compos Struct* 2023; 307: 116626.
139. Mahato B, Lomov S, Akhatov I, et al. Micro-CT based assessment of 3D braided Al2O3 reinforcement uniformity and permeability of all-oxide ceramic matrix composites production processes. In: *20th European Conference on Composite Materials* (ed Anastasios PV and Véronique M), Lausanne, Switzerland, 26-30, June 2022.
140. De Pascalis F, Lionetto F, Maffezzoli A, et al. A general approach to calculate the stiffness tensor of short-fiber composites using the fabric tensor determined by X-ray computed tomography. *Polym Compos* 2023; 44: 917–931.
141. Şık A, Tanabi H, Çubukçu HE, et al. Experimental and analytical investigation of the tensile behavior of 3D-printed composites based on micro-CT analysis. *J Thermoplast Compos Mater* 2024; 37: 2356–2376.
142. Karamov R, Martulli LM, Kerschbaum M, et al. Micro-CT based structure tensor analysis of fibre orientation in random fibre composites versus high-fidelity fibre identification methods. *Compos Struct* 2020; 235: 111818.
143. Krause M, Hausherr J-M, Burgeth B, et al. Determination of the fibre orientation in composites using the structure tensor and local X-ray transform. *J Mater Sci* 2010; 45: 888–896.
144. Mokarizadehhaghighishirazi M, Buffel B, Lomov SV, et al. Homogenisation of the local thermal conductivity in injection-moulded short fibre reinforced composites. *Polymers (Basel)* 2022; 14: 3360.
145. Chapelle L, Lyckegaard A, Kusano Y, et al. Determination of the fibre orientation distribution of a mineral wool network and prediction of its transverse stiffness using X-ray tomography. *J Mater Sci* 2018; 53: 6390–6402.
146. Denos BR, Sommer DE, Favaloro AJ, et al. Fiber orientation measurement from mesoscale CT scans of prepreg platelet molded composites. *Compos A* 2018; 114: 241–249.
147. Martulli LM, Muyshondt L, Kerschbaum M, et al. Carbon fibre sheet moulding compounds with high in-mould flow:

linking morphology to tensile and compressive properties. *Compos A* 2019; 126: 105600.
148. Wan Y, Straumit I, Takahashi J, et al. Micro-CT analysis of internal geometry of chopped carbon fiber tapes reinforced thermoplastics. *Compos A* 2016; 91: 211–221.
149. Wan Y, Straumit I, Takahashi J, et al. Micro-CT analysis of the orientation unevenness in randomly chopped strand composites in relation to the strand length. *Compos Struct* 2018; 206: 865–875.
150. Moll P, Wang S, Coutandin S, et al. Fiber orientation measurement of fiber injection molded nonwovens by image analysis. *Text Res J* 2021; 91: 664–680.
151. Ojanen SP, Finnila MAJ, Herzog W, et al. Micro-computed tomography-based collagen orientation and anisotropy analysis of rabbit articular cartilage. *Ann Biomed Eng* 2023; 51: 1769–1780.
152. Kowalski WJ, Yuan F, Nakane T, et al. Quantification of cardiomyocyte alignment from three-dimensional (3D) confocal microscopy of engineered tissue. *Microsc Microanal* 2017; 23: 826–842.
153. Tsai SW. *Theory of composites design*. Dayton: Think composites, 1992.
154. Chamis CC. Simplified composite micromechanics equations for hygral, thermal and mechanical properties. In: *Ann Conf of the Society of the Plastics Industry (SPI) Reinforced Plastics/Composites Inst*, 1983.
155. Chamis CC. Mechanics of composite materials: past, present, and future. *Compos Technol Res* 1989; 11: 3–14.
156. Clyne TW and Withers PJ. *An introduction to metal matrix composites*. Cambridge: Cambridge University Press, 1993.
157. Kachanov M and Sevostianov I. *Micromechanics of materials, with applications*. Switzerland: Springer Cham , 2018.
158. González C and LLorca J. Mechanical behavior of unidirectional fiber-reinforced polymers under transverse compression: microscopic mechanisms and modeling. *Compos Sci Technol* 2007; 67: 2795–2806.
159. Watanabe T, Kawagoe Y, Hoshikawa Y, et al. Multiscale model for bottom-up prediction of failure parameters of unidirectional carbon-fiber-reinforced composite lamina from the atomic to filament-scales, and its application to failure modeling of open-hole quasi-isotropic composite laminates. *IJSS* 2025; 308: 113130.
160. Yokozeki T, Ogihara S, Yoshida S, et al. Simple constitutive model for nonlinear response of fiber-reinforced composites with loading-directional dependence. *Compos Sci Technol* 2007; 67: 111–118.
161. Sencu R, Yang Z, Wang Y, et al. Multiscale image-based modelling of damage and fracture in carbon fibre reinforced polymer composites. *Compos Sci Technol* 2020; 198: 108243.
162. Sakata S, Ashida F and Enya K. A microscopic failure probability analysis of a unidirectional fiber reinforced composite material via a multiscale stochastic stress analysis for a microscopic random variation of an elastic property. *Comput Mater Sci* 2012; 62: 35–46.
163. Maimí P, Camanho PP, Mayugo J, et al. A continuum damage model for composite laminates: part I–constitutive model. *Mech Mater* 2007; 39: 897–908.
164. Evans E, Brooks R, Liu J, et al. Comparison of X-ray computed tomography and ultrasonic C-scan techniques and numerical modelling of impact damage in a CFRP composite laminate. *Appl Compos Mater* 2024; 31: 249–264.
165. Wan A, Shi J and Li D. Experimental and numerical investigation on tension–tension fatigue behavior of three-dimensional five-directional hybrid braided composites. *Int J Fatigue* 2024; 178: 107975.
166. Dally T, Bilgen C, Werner M, et al. 1: Cohesive elements or phase-field fracture: which method is better for dynamic fracture analyses?. In: Valdman J and Marcinkowski L (eds) *Modeling and simulation in engineering-selected problems*. London: IntechOpen, 2020.
167. Motamedi D and Mohammadi S. Fracture analysis of composites by time independent moving-crack orthotropic XFEM. *IJMS* 2012; 54: 20–37.
168. Higuchi R, Yokozeki T, Nishida K, et al. Decoupled two-scale simulation of damping vibration of composite laminates using image-based periodic representative volume element. *J Sound Vib* 2024; 571: 118096.
169. Karamov R, Lomov SV, Sergeichev I, et al. Inpainting micro-CT images of fibrous materials using deep learning. *Comput Mater Sci* 2021; 197: 110551.
170. Syerko E, Schmidt T, May D, et al. Benchmark exercise on image-based permeability determination of engineering textiles: microscale predictions. *Compos A* 2023; 167: 107397.
171. Liu Q, Gorbatikh L and Lomov SV. A combined use of embedded and cohesive elements to model damage development in fibrous composites. *Compos Struct* 2019; 223: 110921.
172. Lu F, Liu Q, Druzhinin P, et al. Reduction of the volume redundancy in combined embedded elements/cohesive zone modelling-Comments on the paper: Liu Q, Gorbatikh L, Lomov SV. A combined use of embedded and cohesive elements to model damage development in fibrous composites, Composite Structures, 2019, 223: 110921. *Compos Struct* 2019; 226: 111273. doi:10.1016/j.compstruct.2019.111273
173. Yu F, Chen S, Viisainen J, et al. A macroscale finite element approach for simulating the bending behaviour of biaxial fabrics. *Compos Sci Technol* 2020; 191: 108078.
174. Gondrom S, Zhou J, Maisl M, et al. X-ray computed laminography: an approach of computed tomography for applications with limited access. *Nucl Eng Des* 1999; 190: 141–147.
175. Kanouté P, Boso D, Chaboche J-L, et al. Multiscale methods for composites: a review. *Arch Comput Methods Eng* 2009; 16: 31–75.
176. Ostoja-Starzewski M. Material spatial randomness: from statistical to representative volume element. *PrEM* 2006; 21: 112–132.
177. Yan S, Zeng X and Long A. Meso-scale modelling of 3D woven composite T-joints with weave variations. *Compos Sci Technol* 2019; 171: 171–179.
178. Gommer F, Brown LP and Brooks R. Quantification of meso-scale variability and geometrical reconstruction of a textile. *J Compos Mater* 2016; 50: 3255–3266.
179. Rinaldi RG, Blacklock M, Bale H, et al. Generating virtual textile composite specimens using statistical data from micro-computed tomography: 3D tow representations. *J Mech Phys Solids* 2012; 60: 1561–1581.
180. Tao W, Zhu P, Xu C, et al. Uncertainty quantification of mechanical properties for three-dimensional orthogonal woven composites. Part I: stochastic reinforcement geometry reconstruction. *Compos Struct* 2020; 235: 111763.

181. Vanaerschot A, Panerai F, Cassell A, et al. Stochastic characterisation methodology for 3-D textiles based on microtomography. *Compos Struct* 2017; 173: 44–52.
182. Colin D, Bel S, Hans T, et al. Virtual description of noncrimp fabrics at the scale of filaments including orientation variability in the fibrous layers. *Appl Compos Mater* 2020; 27: 337–355.
183. Faes J, Rezaei A, Van Paepegem W, et al. Accuracy of 2D FE models for prediction of crack initiation in nested textile composites with inhomogeneous intra-yarn fiber volume fractions. *Compos Struct* 2016; 140: 11–20.
184. Liu Z, Ge J, Liu K, et al. High-fidelity modeling of 3D woven composites considering inhomogeneous intra-yarn fiber volume fractions. *Compos Struct* 2022; 290: 115505.
185. Farhat C, Lesoinne M, LeTallec P, et al. FETI-DP: a dual–primal unified FETI method—part I: a faster alternative to the two-level FETI method. *IJNME* 2001; 50: 1523–1544.
186. Mandel J. Balancing domain decomposition. *CNME* 1993; 9: 233–241.
187. Bovet C, Parret-Fréaud A, Spillane N, et al. Adaptive multipreconditioned FETI: scalability results and robustness assessment. *Comput Struct* 2017; 193: 1–20.
188. Spillane N, Dolean V, Hauret P, et al. Abstract robust coarse spaces for systems of PDEs via generalized eigenproblems in the overlaps. *NuMat* 2014; 126: 741–770.
189. Yvonnet J and Bonnet G. A consistent nonlocal scheme based on filters for the homogenization of heterogeneous linear materials with non-separated scales. *IJSS* 2014; 51: 196–209.
190. El Said B, Ivanov D, Long AC, et al. Multi-scale modelling of strongly heterogeneous 3D composite structures using spatial voronoi tessellation. *J Mech Phys Solids* 2016; 88: 50–71.
191. Mazars V, Caty O, Couégnat G, et al. Damage investigation and modeling of 3D woven ceramic matrix composites from X-ray tomography in-situ tensile tests. *Acta Mater* 2017; 140: 130–139.
192. Mazars V, Couégnat G, Caty O, et al. Multi-scale damage modeling of 3D ceramic matrix composites from in-situ X-ray tensile tests. In: *18th European Conference on Composite Materials (ECCM18)* (eds Simon W and Abdulghani M), Athens, Greece, 24–28 June 2018, pp. 24–28.
193. Selvaraj J and El Said B. Multiscale modelling of strongly heterogeneous materials using geometry informed clustering. *IJSS* 2023; 280: 112369.
194. Zhang S, Dong C, Zhang H, et al. Analysis method of nonperiodic CMC structure based on super-element. *Ceram Int* 2024; 50: 21611–21618.
195. Abdulle A and Nonnenmacher A. Adaptive finite element heterogeneous multiscale method for homogenization problems. *CMAME* 2011; 200: 2710–2726.
196. Efendiev Y, Galvis J and Hou TY. Generalized multiscale finite element methods (GMsFEM). *J Comput Phys* 2013; 251: 116–135.
197. Jayet T-D, Baranger E, Couegnat G, et al. Feasibility of a weakly intrusive generalized finite element method implementation in a commercial code: application to ceramic matrix composite micro-structures. *Comput Struct* 2021; 242: 106374.
198. Le MV, Yvonnet J, Feld N, et al. The coarse mesh condensation multiscale method for parallel computation of heterogeneous linear structures without scale separation. *CMAME* 2020; 363: 112877.
199. Woo K and Whitcomb J. Global/local finite element analysis for textile composites. *J Compos Mater* 1994; 28: 1305–;1321.
200. El Said B, Daghia F, Ivanov D, et al. An iterative multiscale modelling approach for nonlinear analysis of 3D composites. *IJSS* 2018; 132: 42–58.
201. Wangermez M, Allix O, Guidault P-A, et al. Interface coupling method for the global–local analysis of heterogeneous models: a second-order homogenization-based strategy. *CMAME* 2020; 365: 113032.
202. Yan S, Zou X, Ilkhani M, et al. An efficient multiscale surrogate modelling framework for composite materials considering progressive damage based on artificial neural networks. *Compos B* 2020; 194: 108014.
203. Omairey SL, Dunning PD and Sriramula S. Multiscale surrogate-based framework for reliability analysis of unidirectional FRP composites. *Compos B* 2019; 173: 106925.
204. Satria Palar P, Rizki Zuhal L and Shimoyama K. Gaussian Process surrogate model with composite kernel learning for engineering design. *AIAA J* 2020; 58: 1864–1880.
205. Haeri A and Fadaee MJ. Efficient reliability analysis of laminated composites using advanced kriging surrogate model. *Compos Struct* 2016; 149: 26–32.
206. Wu L, Adam L and Noels L. Micro-mechanics and data-driven based reduced order models for multi-scale analyses of woven composites. *Compos Struct* 2021; 270: 114058.
207. Borkowski L, Skinner T and Chattopadhyay A. Woven ceramic matrix composite surrogate model based on physics-informed recurrent neural network. *Compos Struct* 2023; 305: 116455.
208. Kim H, Jeong I, Cho H, et al. Surrogate model based on data-driven model reduction for inelastic behavior of composite microstructure. *Int J Aeronaut Space Sci* 2023; 24: 732–752.
209. Naresh K, Khan K, Umer R, et al. The use of X-ray computed tomography for design and process modeling of aerospace composites: a review. *Mater Des* 2020; 190: 108553.
210. Vila J, Sket F, Wilde F, et al. An in situ investigation of microscopic infusion and void transport during vacuum-assisted infiltration by means of X-ray computed tomography. *Compos Sci Technol* 2015; 119: 12–19.
211. Wang Y and Sun X. Digital-element simulation of textile processes. *Compos Sci Technol* 2001; 61: 311–319.
212. Badel P, Vidal-Sallé E, Maire E, et al. Simulation and tomography analysis of textile composite reinforcement deformation at the mesoscopic scale. *Compos Sci Technol* 2008; 68: 2433–2440.
213. Syerko E, Schmidt T, May D, et al. Mesoscale results from the virtual permeability benchmark on engineering textiles. In: *21st European Conference on Composite Materials*, 2024, pp.1312–1320.
214. Guo X, Liu R, Wang J, et al. 3D Actual microstructure-based modeling of non-isothermal infiltration behavior and void formation in liquid composite molding. *Appl Math Model* 2021; 94: 388–402.
215. Vignoles GL, Germain C, Coindreau O, et al. Fibre-scale modeling of C/C processing by chemical vapour infiltration using Xray CMT images and random walkers. *ECS Trans* 2009; 25: 1275.
216. Vignoles G. Modeling of chemical vapor infiltration processes. In: *Advances in composites manufacturing and process design*. Cambridge: Elsevier, 2015, pp. 415–458.
217. Catalanotti G and Sebaey TA. An algorithm for the generation of three-dimensional statistically representative volume

elements of unidirectional fibre-reinforced plastics: focusing on the fibres waviness. *Compos Struct* 2019; 227: 111272.
218. Auenhammer RM, Mikkelsen LP, Asp LE, et al. Automated X-ray computer tomography segmentation method for finite element analysis of non-crimp fabric reinforced composites. *Compos Struct* 2021; 256: 113136.
219. Polyzos E, Nikolaou C, Polyzos D, et al. Direct modeling of the elastic properties of single 3D printed composite filaments using X-ray computed tomography images segmented by neural networks. *Addit Manuf* 2023; 76: 103786.
220. He D, Sivakumar S, Xu J, et al. Damage evolution in multi-layer braided composite tubes under torsion studied by in-situ X-ray computed tomography (CT). In: *21st European Conference on Composite Materials*, 2024, pp. 206–211.
221. Liu X, Zhang D, Sun J, et al. Refine reconstruction and verification of meso-scale modeling of three-dimensional five-directional braided composites from X-ray computed tomography data. *Compos Struct* 2020; 245: 112347.
222. Sharma R, Mahajan P and Mittal RK. Image based finite element analysis of 3D-orthogonal carbon-carbon (C/C) composite. In: *World Congress on Engineering 2010* (ed Ao S-I), London, UK, June 30 to July 2 2010, pp.1597–1601.
223. Alghamdi A, Mummery P and Sheikh M. Multi-scale 3D image-based modelling of a carbon/carbon composite. *Modell Simul Mater Sci Eng* 2013; 21: 085014.
224. Gao X, Han X and Song Y. X-ray computed tomography based microstructure reconstruction and numerical estimation of thermal conductivity of 2.5 D ceramic matrix composite. *Ceram Int* 2017; 43: 9790–9797.
225. Zahid M, Sharma R, Bhagat AR, et al. Micro-structurally informed finite element analysis of carbon/carbon composites for effective thermal conductivity. *Compos Struct* 2019; 226: 111221.
226. Lopez E, Gonzalez D, Aguado JV, et al. Manifold Learning Approach for Integrated Computational Materials Engineering. *Arch Comput Methods Eng* 2018; 25: 59–68.
227. Gou J-J, Zhang H, Dai Y-J, et al. Numerical prediction of effective thermal conductivities of 3D four-directional braided composites. *Compos Struct* 2015; 125: 499–508.
228. Sinchuk Y, Pannier Y, Gueguen M, et al. Computed-tomography based modeling and simulation of moisture diffusion and induced swelling in textile composite materials. *IJSS* 2018; 154: 88–96.
229. Sinchuk Y, Pannier Y, Antoranz-Gonzalez R, et al. Analysis of moisture diffusion induced stress in carbon/epoxy 3D textile composite materials with voids by μ-CT based finite element models. *Compos Struct* 2019; 212: 561–570.
230. Cao B, Wang J, Tang S, et al. Experimental and numerical study on moisture diffusion behavior of 3D woven composite. *Compos A* 2024; 185: 108280.
231. Bellezza G, Couégnat G, Ricchiuto M, et al. A 2D image-based multiphysics model for lifetime evaluation and failure scenario analysis of self-healing ceramic-matrix mini-composites under a tensile load. *J Eur Ceram Soc* 2022; 42: 6391–6403.
232. Kim D-W, Lim JH, Kim S-W, et al. Micro-computed tomography-aided modeling for misaligned and noncircular fibers of unidirectional composites and validation under a transverse tensile loading. *Compos Sci Technol* 2021; 212: 108879.
233. Li Y, Ruan X, Akiyama M, et al. Modelling method of fibre distribution in steel fibre reinforced concrete based on X-ray image recognition. *Compos B* 2021; 223: 109124.
234. Lim HJ, Choi H and Yun GJ. Multiscale failure and damage analysis of sheet molding compound (SMC) composites using micro-CT image-based reconstruction model. *Compos B* 2022; 231: 109593.
235. Liu T, Fan C, Ke Z, et al. A real micro-structural model to simulate the transversal compression behaviors of unidirectional composites based on the μ-CT detection. *Compos Commun* 2022; 32: 101184.
236. Wan Y and Takahashi J. Mechanical modeling of CF/PA6 sheet molding compounds with X-ray computed tomography-based internal geometry considerations. *Compos Sci Technol* 2020; 192: 108104.
237. Ai S, Song W and Chen Y. Stress field and damage evolution in C/SiC woven composites: image-based finite element analysis and in situ X-ray computed tomography tests. *J Eur Ceram Soc* 2021; 41: 2323–2334.
238. Wang Z, Zhang L, Zhong J, et al. Image-Based peridynamic modeling-based micro-CT for failure simulation of composites. *Materials (Basel)* 2024; 17: 4987.
239. Ren W, Yang Z, Sharma R, et al. Two-dimensional X-ray CT image based meso-scale fracture modelling of concrete. *Eng Fract Mech* 2015; 133: 24–39.
240. Saleh MN, Lubineau G, Potluri P, et al. Micro-mechanics based damage mechanics for 3D orthogonal woven composites: experiment and numerical modelling. *Compos Struct* 2016; 156: 115–124.
241. Pei S, Wang K, Li J, et al. Mechanical properties prediction of injection molded short/long carbon fiber reinforced polymer composites using micro X-ray computed tomography. *Compos A* 2020; 130: 105732.
242. Yang Z, Ren W, Sharma R, et al. In-situ X-ray computed tomography characterisation of 3D fracture evolution and image-based numerical homogenisation of concrete. *Cem Concr Compos* 2017; 75: 74–83.
243. Huang Y, Yang Z, Ren W, et al. 3D meso-scale fracture modelling and validation of concrete based on in-situ X-ray computed tomography images using damage plasticity model. *IJSS* 2015; 67: 340–352.
244. Gao Y, Hu W, Xin S, et al. A review of applications of CT imaging on fiber reinforced composites. *J Compos Mater* 2022; 56: 133–164.
245. Wang Y, Chai Y, Soutis C, et al. Evolution of kink bands in a notched unidirectional carbon fibre-epoxy composite under four-point bending. *Compos Sci Technol* 2019; 172: 143–152.
246. Scott A, Mavrogordato M, Wright P, et al. In situ fibre fracture measurement in carbon–epoxy laminates using high resolution computed tomography. *Compos Sci Technol* 2011; 71: 1471–1477.
247. Chai Y, Wang Y, Yousaf Z, et al. Damage evolution in braided composite tubes under torsion studied by in-situ X-ray computed tomography. *Compos Sci Technol* 2020; 188: 107976.
248. Chai Y, Wang Y, Yousaf Z, et al. Following the effect of braid architecture on performance and damage of carbon fibre/epoxy composite tubes during torsional straining. *Compos Sci Technol* 2020; 200: 108451.

249. Bale HA, Haboub A, MacDowell AA, et al. Real-time quantitative imaging of failure events in materials under load at temperatures above 1,600 degrees C. *Nat Mater* 2013; 12: 40–46.
250. Turpin L, Roux S, Caty O, et al. In situ tomographic study of a 3D-woven SiC/SiC composite part subjected to severe thermo-mechanical loads. *J Synchrotron Radiat* 2022; 29: 522–531.
251. Wang Y, Xu X, Zhao W, et al. Damage accumulation during high temperature fatigue of Ti/SiCf metal matrix composites under different stress amplitudes. *Acta Mater* 2021; 213: 116976.
252. Yu B, Blanc R, Soutis C, et al. Evolution of damage during the fatigue of 3D woven glass-fibre reinforced composites subjected to tension–tension loading observed by time-lapse X-ray tomography. *Compos A* 2016; 82: 279–290.
253. Scott A, Sinclair I, Spearing S, et al. Damage accumulation in a carbon/epoxy composite: comparison between a multiscale model and computed tomography experimental results. *Compos A* 2012; 43: 1514–1522.
254. Chen Y, Gélébart L, Chateau C, et al. Analysis of the damage initiation in a SiC/SiC composite tube from a direct comparison between large-scale numerical simulation and synchrotron X-ray micro-computed tomography. *IJSS* 2019; 161: 111–126.
255. Mehdikhani M, Aravand M, Sabuncuoglu B, et al. Full-field strain measurements at the micro-scale in fiber-reinforced composites using digital image correlation. *Compos Struct* 2016; 140: 192–201.
256. Mehdikhani M, Steensels E, Standaert A, et al. Multi-scale digital image correlation for detection and quantification of matrix cracks in carbon fiber composite laminates in the absence and presence of voids controlled by the cure cycle. *Compos B* 2018; 154: 138–147.
257. Van Vlierberghe E, Gayot S, Klavzer N, et al. Microstructural strain localisation phenomena in fibre-reinforced polymer composites: insights from nanoscale digital image correlation and finite element modelling. *Compos Sci Technol* 2024; 258: 110842.
258. Janeliukstis R and Chen X. Review of digital image correlation application to large-scale composite structure testing. *Compos Struct* 2021; 271: 114143.
259. Bay BK. Methods and applications of digital volume correlation. *J Strain Anal Eng Des* 2008; 43: 745–760.
260. Buljac A, Jailin C, Mendoza A, et al. Digital volume correlation: review of progress and challenges. *Exp Mech* 2018; 58: 661–708.
261. Mehdikhani M, Breite C, Swolfs Y, et al. Digital volume correlation for meso/micro in-situ damage analysis in carbon fiber reinforced composites. *Compos Sci Technol* 2021; 213: 108944.
262. Holmes J, Sommacal S, Das R, et al. Digital image and volume correlation for deformation and damage characterisation of fibre-reinforced composites: a review. *Compos Struct* 2023; 315: 116994.
263. Hild F and Roux S. Comparison of local and global approaches to digital image correlation. *Exp Mech* 2012; 52: 1503–1519.
264. Avril S, Bonnet M, Bretelle A-S, et al. Overview of identification methods of mechanical parameters based on full-field measurements. *Exp Mech* 2008; 48: 381–402.
265. Roux S and Hild F. Optimal procedure for the identification of constitutive parameters from experimentally measured displacement fields. *IJSS* 2020; 184: 14–23.
266. Bertin M, Hild F, Roux S, et al. Integrated digital image correlation applied to elastoplastic identification in a biaxial experiment. *J Strain Anal Eng Des* 2016; 51: 118–131.
267. Archer T, Berny M, Beauchêne P, et al. Creep behavior identification of an environmental barrier coating using full-field measurements. *J Eur Ceram Soc* 2020; 40: 5704–5718.
268. Turpin L, Roux S, Caty O, et al. Coupling tomographic and thermographic measurements for in-situ thermo-mechanical tests. *Meas Sci Technol* 2020; 32: 035401.
269. Gras R, Leclerc H, Hild F, et al. Identification of a set of macroscopic elastic parameters in a 3D woven composite: uncertainty analysis and regularization. *IJSS* 2015; 55: 2–16.
270. Turpin L, Neggers J, Mendoza A, et al. Identification of the effective interface between the homogenized phases of a dual-weave 3D composite. *Eur J Mech-A/Solids* 2024; 103: 105166.
271. García-Moreno F, Kamm PH, Neu TR, et al. Tomoscopy: time-resolved tomography for dynamic processes in materials. *Adv Mater* 2021; 33: e2104659.
272. Maire E, Bonnard G, Adrien J, et al. Dual beam microfocus high-energy tomography: towards multimodal and faster laboratory experiments. *Tomogr Mater Struct* 2024; 5: 100030.
273. Leclerc H, Roux S and Hild F. Projection savings in CT-based digital volume correlation. *Exp Mech* 2015; 55: 275–287.
274. Jailin C, Buljac A, Bouterf A, et al. Fast 4D tensile test monitored via X-CT: single projection based digital volume correlation dedicated to slender samples. *J Strain Anal Eng Des* 2018; 53: 473–484.